Functional consequences of a p53-MDM2-p21 incoherent feedforward loop

Jamie A. Dean[1,2,3,4,5,*], Jose Reyes[6,7], Michael Tsabar[6,8], Ashwini Jambhekar[6,8], Galit Lahav[6,8], and Franziska Michor[1,2,3,8,9,10,11,*]

[1]Department of Data Science, Dana-Farber Cancer Institute, Boston, MA, USA
[2]Department of Stem Cell and Regenerative Biology, Harvard University, Cambridge, MA, USA
[3]Department of Biostatistics, Harvard T.H. Chan School of Public Health, Boston, MA, USA
[4]Department of Medical Physics and Biomedical Engineering, University College London, London, United Kingdom
[5]Institute for the Physics of Living Systems, University College London, London, United Kingdom
[6]Department of Systems Biology, Harvard Medical School, Boston, MA, USA
[7]Memorial Sloan Kettering Cancer Center, New York, NY, USA
[8]The Ludwig Center at Harvard, Boston, MA, USA
[9]Center for Cancer Evolution, Dana-Farber Cancer Institute, Boston, MA, USA
[10]The Broad Institute of MIT and Harvard, Cambridge, MA, USA
[11]Lead contact
*Correspondence: jamie.dean@ucl.ac.uk (J.A.D.), michor@jimmy.harvard.edu (F.M.)

Summary

Genetically identical cells can respond heterogeneously to cancer therapy, with a subpopulation of cells often entering a temporarily arrested treatment-tolerant state before repopulating the tumor. To investigate how heterogeneity in the cell cycle arrest protein p21 arises, we imaged the dynamics of p21 transcription and protein expression along with those of p53, its transcriptional regulator, in single cells using live cell fluorescence microscopy. Surprisingly, we found that the rate of p21 transcription depends on the change in p53 rather than its absolute level. Through combined theoretical and experimental modeling, we determined that p21 transcription is governed by an incoherent feedforward loop mediated by MDM2. This network architecture facilitates rapid induction of p21 expression and variability in p21 transcription. Abrogating the feedforward loop overcomes rapid S-phase p21 degradation, with cells transitioning into a quiescent state that transcriptionally resembles a treatment-tolerant persister state. Our findings have important implications for therapeutic strategies based on activating p53.

Introduction

Genetically identical populations of cells often exhibit heterogeneous fates in response to the same environmental exposures. Such non-genetic variability in cell fates represents a major challenge for cancer therapy aiming to eliminate all tumor cells, facilitating the survival of some cells in an otherwise treatment-sensitive population[1]. This non-genetic resistance can occur through a subpopulation of cells transiently entering a cell cycle-arrested state, during which they are able to tolerate therapies that target rapidly proliferating cells[2–5], including radiation and chemotherapy, before re-entering a proliferative state to repopulate the tumor. So-called cancer "persister" cells are now increasingly thought to be a substantial source of treatment failures in oncology and, hence, there is a pressing need to develop novel treatment approaches to overcome this form of resistance. To realize these new therapeutic strategies, an improved understanding of non-genetic resistance mechanisms is required. Knowledge of mechanisms underlying variability in cell cycle phase transitions could also inform approaches to protect normal cells from anti-cancer therapies and reduce treatment side effects.

Previous work has shown that variability in cell fates can be explained by variability in the dynamics of transcription factors regulating fate-determining genes. Different stimuli can give rise to differences in the dynamics of the same transcription factor and result in divergent cell fates. For example, the levels of p53, a key transcription factor regulating the response to DNA damage, oscillate in response to ionizing radiation (IR) cells, but exhibit a sustained increase in response to ultraviolet (UV) radiation[6]. These different patterns of p53 expression dynamics are associated with different fates: senescence and apoptosis, respectively. However, even when cells are exposed to the same treatment and exhibit the same broad patterns of transcription factor dynamics, subtle variability in those dynamics can explain cell fate variability. Such subtle non-genetic intercellular heterogeneity in the dynamics of p53 can explain whether cells die or survive following treatment with cisplatin chemotherapy[7].

Cell cycle arrest is primarily controlled by the cyclin-dependent kinase inhibitor, *CDKN1A* (p21), which is transcriptionally activated by p53 in response to DNA damage[8–12]. Entry and exit of cell cycle arrest is controlled by a bistable switch created by double negative feedback between p21 and CDK2[13,14]. Noise in p53 protein levels propagates to p21 protein levels and plays a role in cell fate heterogeneity, in particular the ability of cells to enter and escape from cell cycle arrest[13,15,16].

Given the importance of p21 expression dynamics in cell fate determination and heterogeneity in p21 dynamics on non-genetic variability in treatment response[17], we sought to quantitatively characterize p21 expression dynamics through integrating single cell timelapse fluorescence microscopy of p21 and p53 and mathematical modeling of the regulation of and noise propagation through this circuit.

Results

Transcription of p21 is dependent on the change in p53 rather than its absolute level

To quantitatively characterize p53-dependent p21 expression, we used a recently developed experimental system to study the dynamics of the p53 and p21 proteins (using fluorescent reporters p53-CFP and p21-mCherry) together with the dynamics of p21 transcription (using the MS2 system) in single MCF-7 breast cancer epithelial cells[18]. We treated cells with IR (a single dose of either 10 Gy, 5 Gy or 2.5 Gy) and imaged them with time-lapse microscopy for approximately 2 days. As previously described[19], p53 protein levels oscillated, with a period of approximately 5.5 h, in response to IR (Figures 1A and S1A). The p53 oscillations resulted in bursts of p21 transcription (Figures 1B and S1B) and p21 protein accumulation (Figures 1C and S1C).

When visualizing the dynamics of p53 and p21 transcription simultaneously in single cells, we observed that p21 transcription occurred only at the times corresponding to the peaks of the p53 oscillations (Figures S1D-G). This observation suggested that p21 transcriptional output is dependent on the change in p53 rather than its absolute concentration. However, longer-term trends of increasing and decreasing p53, which are present in the signal, may represent technical artifacts, rather than true p53 dynamics, confounding the interpretation. Therefore, before quantitatively investigating p53-dependent p21 transcription, we detrended the raw p53 dynamics data (Figures 1D and S1H-I) to minimize these trends.

To formally test the hypothesis that p21 transcription is dependent on the change in p53, we developed two different statistical models that predict p21 transcription based on p53 protein expression: one based on the absolute level of p53 (Figure 1D) and a second based on the change in p53 level (Figure 1E). To infer when the p21 gene was in the “ON” and “OFF” states, we fit a two-state hidden Markov model to the p21-MS2 time course data for each cell, estimating for each time point whether the gene is in the “ON” or “OFF” state (Figure 1F). We then fit logistic regression models of the inferred p21 gene state based on either the absolute (detrended) p53 level (Figure 1G), or the change in (detrended) p53 level (Figure 1H). We subsequently compared the predictive performance of the models for each cell, as assessed by the area under the receiver operating characteristic curve (AUC). We found that while the model based on the absolute p53 levels were able to partially predict p21 transcription (mean AUC = 0.63), the model based on the change in p53 was substantially superior (mean AUC = 0.82; (Figure 1I; $p < 2.2E-16$, paired Wilcoxon test). We repeated this analysis using data from an additional experiment employing the same reporter system, but a shorter time course of 15 h and a higher temporal resolution of 2 minutes[18], to minimize the increasing and decreasing p53 trends apparent in the original experiment. Again, p21 transcription was significantly better predicted by the change in p53 (mean AUC = 0.87) than the absolute p53 level (mean AUC = 0.66; Figure S1H; $p < 2.2E-16$, paired t-test). This finding suggests that p21 transcription is not solely dependent on p53 concentration, but is instead under the control of a more complex regulatory mechanism capable of parsing the change in p53 expression.

Transcription of p21 is governed by an incoherent feedforward loop that enables p53 change detection

We next investigated how the change in p53 could be parsed by the p21 promoter. Change detection cannot be achieved by a two-node network, such as a network consisting of only a p53 node and a p21 node; instead, the simplest gene network capable of change detection is a three-node network. An incoherent type-1 feedforward loop (IFFL) is a 3-node network that facilitates fold-change detection in other transcriptional systems, including NF-κB[20] and TGF-β[21]. We observed that p21 transcription displayed an ultrasensitive response, i.e. a rapid switching on and off of p21 transcriptional bursting as opposed to a gradual “ramp up” and “ramp down” (Figures 1B, S1E, S1G). This behavior suggests that the transcription of p21 is governed by a molecular titration mechanism, whereby p21 is transcribed when the concentration of p53 is above that of a negative regulator of p21 transcription. As IFFLs are capable of molecular titration and have previously been identified in gene regulation, we focused on this motif as a potential alternative mechanism of p21 transcription to simple positive regulation (PR) by p53.

To formally compare alternative mechanisms of p21 transcription, namely PR and IFFL, we constructed stochastic mathematical models of each (Figures 2A-B; Materials and Methods). For these models we did not commit to an explicit functional form to describe the p53 dynamics to minimize the number of assumptions; instead, we used the p53 data as input into the models. We simulated p21 transcription dynamics from our two stochastic models for each single cell in our data using the Gillespie stochastic simulation algorithm (Figures 2C-D) and compared the model simulations to our data by computing the p21-MS2 autocorrelation function (Figures 2E-F) and the p53 - p21-MS2 cross-correlation function (Figures 2G-H). This approach takes advantage of the fact that our experimental data captures the transcription factor and transcription dynamics over time in the same single cells. We fit both models to our experimental measurements using approximate Bayesian computation-based inference, repeating the stochastic simulations for all cells for 5,000 combinations of different parameter values, to determine which model could best explain the data (Materials and Methods). We found that none of the correlation functions generated by the PR model simulations were able to match the correlation functions in the data from the long (Figures 2I-J, S2A-B and S2E-F) or short time course experiments (Figures S2I-J), whereas the IFFL model recapitulated these correlation functions well (Figures 2K-L, S2C-D and S2G-H). Our Bayesian model selection procedure indicated that the IFFL model provided the best fit to the data for all the dose levels and datasets (posterior probability of the IFFL model and not the PR model = 1.0, 1.0, 0.98 and 1.0 for the 10 Gy, 5 Gy, 2.5 Gy long time course datasets and short time course dataset, respectively). Thus, our combined experimental and theoretical modeling approach suggests that transcription of p21 is not governed by simple PR by p53, but instead by an IFFL involving p53 and an additional transcriptional repressor.

The p53-MDM2 interaction is necessary for transcriptional repression of p21

We next attempted to identify the repressor of p21 transcription, representing the third node in the IFFL. We reasoned that the transcriptional repressor should fulfil several criteria: (1) it should be a transcriptional target of p53; (2) it should bind to a regulatory region of the *CDKN1A* gene (either directly or indirectly) and (3) it should have dynamics similar to those predicted by our computational model. Based on fulfilling these criteria, in addition to the fact that MDM2 has previously been shown to perform a role in transcriptional repression of p53 target genes[22–27], including p21[25], we predicted that MDM2 is the transcriptional repressor. We then leveraged our theoretical model to design and analyze an experiment to test this prediction.

Our theoretical model predicts that inhibiting the activity of the repressor would result in the p21 transcription rate being dependent on the absolute abundance of p53 rather than the change in p53 concentration. Given that MDM2 is recruited to genes through binding to p53[27], we reasoned that its predicted transcriptional repressor activity could be inhibited by pharmacologically blocking its binding to p53. To test our model prediction, we performed a validation experiment in which we treated cells with 10 Gy IR alone or in combination with 10 μM nutlin-3a (IR + nutlin-3a), a drug that inhibits the binding of MDM2 to p53[28], and imaged the dynamics of p53 and p21 expression by time-lapse microscopy (Figure S3A-C). As described above, we compared the PR and IFFL model fits to the data by simulation and approximate Bayesian computation. We found that in the IR treated cells the PR model did not fit the data well (Figures 3A-B), whereas the IFFL model did (Figures 3C-D): the Bayesian model selection procedure strongly favored the IFFL model with a posterior probability of the IFFL model (and not the PR model) of 1.0. However, for the cells treated with IR + nutlin-3a, the PR model described the data similarly to the IFFL model (Figures 3E-H) and the posterior probability for the IFFL model was substantially reduced to 0.70. Note that the IFFL model reduces to the PR model when the level of the repressor or its effect are set to 0, which likely explains the preference for this model, although to a much lesser extent, even when the PR model can recapitulate the correlation functions in the data. This observation validates our model prediction.

To further interrogate our proposed mechanism of p21 regulation, we returned to our statistical models of p21 transcription. We found that, for the cells treated with IR alone, the model based on the change in p53 was substantially superior (mean AUC = 0.82) to the one based on absolute level of p53 (mean AUC = 0.64), as before (Figure 3I; $p < 2.2E-16$, paired Wilcoxon test). However, for the cells treated with IR + nutlin-3a, the reverse was true (Figure 3J; p53 level: mean AUC = 0.77; p53 change: mean AUC = 0.63; $p < 2.2E-16$, paired Wilcoxon test). This observation provides further support for our proposed mechanism that the p53-MDM2 interaction is necessary for the transcriptional repression of p21.

The incoherent feedforward loop may confer beneficial functionality

We then sought to elucidate the functional consequences of p21 transcription being governed by an IFFL. Previous theoretical[29] and experimental[30] studies have proposed that the type-1 IFFL increases the response rate of the transcriptional target gene. The capability to rapidly enact cell cycle arrest upon detection of DNA damage would very likely be advantageous to cells. We, therefore, investigated whether this scenario was the case for p21. Experimentally manipulating a system to test the effects of a specific regulatory interaction in isolation, without affecting other properties of the system such as steady state levels, is extremely challenging. However, such a controlled comparison can be achieved using mathematical modeling[31]. We thus employed mathematical modeling to investigate the effects of the IFFL on the p21 response rate. To this end, we modeled the dynamics of p53-dependent p21 protein expression with p21 production governed either by PR or an IFFL (Materials and Methods). We selected the p21 production rates for the two models such that the "pseudo-steady state" levels of p21, i.e. where the time-averaged p21 level remains constant and does not continue to increase with additional p53 pulses, were approximately equal for both models. Using these models, we found that the time taken for p21 protein expression to reach half the value of its pseudo-steady state level for the PR model was approximately 15 h (Figure 4A) while the corresponding time for the IFFL model was 5 h (Figure 4B). The higher p21 induction rate for the IFFL model is due to the production rate of p21 being higher than for the PR model during the time taken for the levels of the repressor to accumulate. This observation suggests that the IFFL indeed increases the rate of p21 induction, which would facilitate rapid cell cycle arrest following DNA damage.

It has also been proposed that the type-1 IFFL generates a large extent of noise[32], which would facilitate cells to enact "bet hedging", a strategy to minimize the risk of population extinction. Consistent with that pattern, p21 has been observed to exhibit substantial heterogeneity in unstressed conditions, reminiscent of bet hedging[14]. Comparing the p21-MS2 noise between cells treated with IR and cells treated with IR + nutlin-3a revealed that inhibiting the p53-MDM2 interaction significantly decreased noise in p21 transcription, when noise was measured by either the Fano factor (standard deviation squared/mean) (Figure 4C) or the coefficient of variation (standard deviation/mean) (Figure S4A). This finding suggests that the IFFL increases p21 noise. However, given that nutlin-3a increases p53 protein stability and reduces p53 protein noise (Figure S4B) the reduction in p21-MS2 noise upon addition of nutlin-3a to IR may be solely due to effects on p53 noise and not the IFFL. We, therefore, compared the ratio of the p21-MS2 noise to the p53 noise and found that the p21-MS2 to p53 protein noise ratio was higher in cells treated with IR than when the IFFL is abrogated through treatment with nutlin-3a when measuring noise using either the Fano factor (Figure 4D) or coefficient of variation (Figure S4C). Both the p21-MS2 noise and p21-MS2 to p53 protein noise ratio were consistent between IR treated cells in the experiments (Figure S4D-E). This observation suggests that MDM2-mediated transcriptional repression of p21 enhances p21 transcriptional noise.

Another potential property of IFFLs is that they enable the transmission of multiple signals in the dynamics of a single transcription factor, known as "signal multiplexing"[33,34], when integrated into a larger network. The dynamics of a single transcription factor could simultaneously encode two signals: one encoded in its absolute level and the other in the change in its level. Target genes whose transcription is governed by PR would decode the signal encoded in the absolute level and those whose transcription is governed by an IFFL would decode the change in transcription factor level. If multiple signals were indeed encoded in p53 dynamics, then we would expect that to decode these signals some p53 transcriptional target genes would be regulated by PR and others by IFFL. To test this hypothesis, we performed a new, mathematical model-based analysis of previously published RNA-seq time course data of p53 transcriptional target genes[35]. Our modelling approach was based on distinguishing between differences in mRNA expression of p53 target genes following treatment with IR and IR + nutlin-3a that were due to differences in p53 levels alone and increases in expression greater than what would be expected based on increased p53 level alone (Figure 4E). We modelled mRNA expression dynamics using ordinary differential equations with transcription governed by either PR or IFFL and performed model comparison individually for each p53 transcriptional target, previously defined based on RNA-seq and TP53 chromatin immunoprecipitation (ChIP)-seq data[35], using approximate Bayesian computation (Figure 4F-G; Materials and Methods). This analysis indicated a high posterior probability that p21 transcription was governed by a MDM2-mediated IFFL (0.88). The agreement of this finding, made from bulk RNA-seq data, with that made from our single cell time-lapse microscopy data validates the suitability of this approach for determining whether the transcription of genes is governed by a MDM2-mediated IFFL. We found that for 22% of p53 transcriptional target genes, mRNA expression dynamics were best described by a MDM2-mediated IFFL model (posterior probability of IFFL model > 0.5), whereas the remaining 78% were best described by a PR model (Figure 4F-G). In addition to p21, the IFFL model was strongly preferred for MDM2 (posterior probability = 0.91). This analysis provides evidence that, for a subset of genes, the addition of nutlin-3a to IR results in gene expression changes that are not solely dependent on changes in p53 dynamics, but also from the alleviation of the MDM2-dependent transcriptional repression of p53 target genes. These findings are consistent with a gene regulatory network structure that can decode a multiplexed signal encoded in p53 dynamics.

To determine whether similar MDM2-mediated transcriptional repression may occur in a subset of p53 target genes in other cell lines, we reanalyzed TP53 and MDM2 ChIP-seq data of four different cell lines from a recent study[36], searching for overlapping TP53 and MDM2 peaks. Such overlapping peaks are likely necessary for MDM2-mediated repression of p53-dependent transcription. Consistent with IFFL regulation of a subset of p53 transcriptional target genes, we found both overlapping and non-overlapping TP53 and MDM2 peaks in all of the cell lines (Figures 4H-I and S4F-G). Three of the 4 cell lines had overlapping TP53 and MDM2 peaks on the *MDM2* gene and none had overlapping TP53 and MDM2 peaks on the *CDKN1A* gene. These observations suggest that the expression of a subset of p53 target genes may be regulated by a MDM2-mediated IFFL, with the IFFL-regulated genes differing between different cells.

It is unclear what determines which p53 target genes have their expression regulated by an IFFL. However, when analyzing the MCF-7 cell TP53 ChIP-seq data, we noted that p53 target genes that were inferred to be IFFL-regulated with high probability, *CDKN1A* and *MDM2*, had a short distance between the TP53 binding site and transcription start site (Figure 4G). We searched for a similar relationship in the TP53 and MDM2 ChIP-seq data and found that the TP53 binding sites for genes bound by both TP53 and MDM2 were significantly closer to the transcription start sites (predominantly in regions designated promoters) than for genes bound by TP53 alone (predominantly in regions designated enhancers) (LPS141 p = 3.5E-9, LPS853 p = 1.2E-13; Figures 4J-K). Co-binding of TP53 and MDM2, facilitating transcriptional repression, may therefore preferentially occur at gene promoters rather than enhancers.

Abrogating MDM2-mediated transcriptional repression of p21 inhibits and reverses the G1-S transition

Therapeutically targeting the interaction between p53 and MDM2 is an active area of research in oncology. This strategy is based on increasing p53 levels of p53 wild-type cancer cells through inhibiting its MDM2-mediated degradation. However, the distinct effects of abrogating the p21 IFFL by inhibiting the p53-MDM2 interaction have not been studied. We therefore investigated the impact of nutlin-3a on p21 expression in more detail. To disentangle the effects of inhibiting MDM2-mediated p53 degradation and MDM2-mediated p21 transcriptional repression on the accumulation of p21, we developed a combined theoretical and experimental modeling approach.

Theoretical modelling of p21 expression dynamics (Materials and Methods) predicts that at pseudo-steady state with high concentrations of p53, the concentration of p21 is given by

$$[p21] \approx \frac{\alpha}{\beta}$$

where α and β are the production and degradation rates of p21, respectively. This relationship indicates that if nutlin-3a only increases p53 levels, without affecting the p21 production rate per unit p53, then when $[\mathrm{p21}]$ is plotted against $[\mathrm{p53}]$ the y-intercepts of IR and IR + nutlin-3a treated cells will be the same. Alternatively, if nutlin-3a increases the production rate of p21 per unit p53, then the y-intercept of IR + nutlin-3a treated cells will be greater than IR treated cells. Beyond detecting qualitative differences, the equation enables the ratio of p21 production and degradation rates to be inferred from measurements of p21 concentration. To test the validity of this theory we plotted experimentally derived values of $[\mathrm{p21}]$ against $[\mathrm{p53}]$ using the data from cells treated with IR and IR + nutlin-3a (Figures S3A-C). We used the data acquired from the final 2.5 h of the experiment when p21 protein levels reach pseudo-steady. The data clustered into two populations of cells for both conditions. This bimodal distribution is expected as p21 has two different degradation rates, with a rapid degradation occurring during S phase and a slower degradation during the remainder of the cell cycle[37], leading to different steady state levels. Indeed, as predicted by the theory, this analysis gave rise to straight lines with slopes of 0 for both conditions (Figures 5A-B). The y-intercepts of the lines differed, with the lines corresponding to the cells treated with IR + nutlin-3a having greater y-intercepts (Figures 5A-B). This observation implies that the addition of nutlin-3a increases the production rate of p21 substantially beyond what would be expected based on the increased levels of p53 alone. This finding provides further evidence to support our finding that MDM2 represses p53-dependent p21 transcription.

To this point our theory allowed us to infer the ratio of the production and degradation rates of p21. Quantifying the p21 production rate, in the presence and absence of nutlin-3a, enables further insights to be gleaned. In particular, previous theoretical models have suggested that the G1-S transition can be reversed by the accumulation of p21 in S-phase, achieved through loss of CDT[38,39], which rapidly degrades p21 during S-phase[37]. We considered that p21 accumulation during S-phase, and hence reversal of the G1-S transition, could also be achieved through increasing its production rate to a level higher than its degradation rate. Therefore, we performed an additional experiment to measure the p21 degradation rate, which would enable inferring the p21 production rates in the context of treatment with IR and IR + nutlin-3a. To measure the rates of p21 protein degradation in single cells, we exposed cells to siRNA targeting either p21 alone or p53 and p21 at 20 h following IR (Figure S5A). This perturbation led to a two-phase decay of p21 (Figure 5C). Initially p21 levels decreased slowly, followed by a rapid decrease, presumably due to cells entering S phase during which $CRL4^{CDT2}$-dependent rapid degradation occurs[37]. We inferred these two different decay rates in all cells (from both conditions) by fitting a piecewise linear regression model to the log-transformed expression level data (Figure 5C). The distribution of p21 degradation rates was bimodal with peak degradation rates (inferred by Gaussian mixture modeling) of 0.16 h^{-1} and 3.09 h^{-1} (Figure 5D), corresponding to half-lives of 4.3 h and 0.2 h. These degradation rates imply, based on the equation for steady state levels of p21, that the production rates under IR and IR + nutlin-3a treatments are 520 a.u.h^{-1} and 4880 a.u.h^{-1}, respectively (Figure 5E).

Having inferred the two different p21 production and degradation rates allowed us to mathematically decouple the effects of MDM2 on p53 levels and p21 production per unit concentration of p53 by computing the levels of p21 under different combinations of production and degradation rates. This analysis suggests that inhibiting MDM2-mediated p53 degradation alone would be insufficient to cause p21 accumulation during S-phase (Figure S5B). However, additionally inhibiting the transcriptional repression of p21 will achieve p21 accumulation in S-phase (Figure 5F). This finding implies that the pharmacological abrogation of the p21 IFFL will lead to cells remaining in or transitioning to the G1 or G0 phases of the cell cycle and that this would not be achieved through increasing p53 alone without abrogating the IFFL.

To test this prediction, we computed cell cycle signature[40] scores for previously published RNA-seq time course data of cells treated with IR alone or IR + nutlin-3a[35] using gene set variation analysis. This analysis indicated that cells treated with IR predominantly arrest at the G2/M checkpoint whereas cells treated with IR + nutlin-3a exit the cell cycle, arresting in G0 (Figure 5G). We reasoned that this dramatic effect on cell cycle progression should also lead to changes in cell morphology associated with cell cycle phase, such as nuclear area. In cells that were treated with IR, the nuclear area increased over time following treatment ($p < 2E-16$, paired t-test; Figures S5C-D), suggestive of cell cycle progression. However, in cells that were treated with IR + nutlin-3a the nuclear area decreased ($p = 7.2E-6$, paired t-test; Figures S5C-D). This observation provides morphological evidence, in addition to the transcriptional evidence, of the divergent fates of cells treated with IR and IR + nutlin-3a. We corroborated this morphological change by confirming that nuclear size transcriptional signatures were decreased following treatment with IR + nutlin-3a, but not IR (Figure S5E). Together these findings suggest that IR causes cells to undergo G2/M arrest, but abrogating the p53-MDM2 interaction alters the fate of the cells to instead enter a G0 arrest. Importantly, while the effects of MDM2 on p53 degradation and transcriptional repression are challenging to experimentally decouple, our theoretical modeling supports the conclusion that the divergence in cell cycle progression is specifically related to the MDM2-dependent transcriptional repression, rather than increased levels of p53 alone.

Abrogating the p53-MDM2 interaction steers cells into a persister state

Having shown that abrogating the IFFL substantially altered p21 dynamics and cell cycle progression, we next sought to investigate the relative contribution of these effects to the global context of p53-mediated changes. We, therefore, compared transcriptome-wide mRNA expression time courses in cells treated with IR in the presence or absence of nutlin-3a using RNA-seq data. Differential expression analyses of mRNA time series data[35] identified 1473 upregulated and 1188 downregulated genes upon addition of nutlin-3a to IR (Figure 6A). This observation is consistent with our previous work showing p53-dependent increases and decreases in expression of different sets of genes following IR treatment in the same cell line[35]. Analysis of the transcriptional regulators of the differentially expressed genes (Materials and Methods) indicated that the upregulated genes were enriched for transcriptional targets of p53 and p63 (Figure 6B), as expected. The downregulated genes were enriched for transcriptional targets of E2F4 and LIN9 (Figure 6C). E2F4 and LIN9 are members of the DREAM complex that represses transcription of cell cycle genes[41] and whose formation is dependent on p21[42]. This finding suggests that inhibiting the interaction between p53 and MDM2 with nutlin-3a increases the levels of p21, activating the DREAM complex and repressing its target genes. The fact that many of the differentially expressed genes are transcriptional targets of E2F4 and LIN9 suggests that p21 plays a major role in the global gene expression changes resulting from inhibiting the p53-MDM2 interaction.

Gene set variation analysis using the Hallmark pathways indicated nutlin-3a-dependent downregulation of E2F and MYC targets and the G2M checkpoint, in addition to the expected upregulation of TP53 (Figure S6A). This observation is consistent with the previously identified antagonistic role of p53 on MYC in breast cancer[43]. MYC is also involved in nuclear size regulation, which may explain our earlier finding of nuclear shrinkage upon treatment with IR + nutlin-3a. Downregulation of DREAM complex target genes and MYC is associated with quiescent states such as embryonic diapause, resistance of normal tissues[44] and cancer cells[45] to therapy and treatment-tolerant persister cells. We, therefore, studied persister cell signatures in our RNA-seq data. We found that, for almost all persister cell signatures, IR + nutlin-3a increased upregulated persister cell signatures and decreased downregulated persister cell signatures (Figure 6D). This finding suggests that adding nutlin-3a to IR shifts cells into a quiescent persister state, in large part mediated through abrogating p21 transcriptional repression, leading to downregulation of DREAM target genes.

Finally, we tested whether the transcriptional differences induced by the addition of nutlin-3a to IR, leading to the alleviation of MDM2-mediated repression of p21 transcription, were associated with treatment resistance, as suggested by the increase in persister cell signature scores. We created two gene signatures, consisting of genes either significantly upregulated or downregulated in IR + nutlin-3a versus IR treated MCF-7 cells (Figure 6A). Both the upregulated and downregulated gene signatures were associated with IR resistance in cell lines from the Cancer Cell Line Encyclopedia[46] (p = 6.4E-6 and 1.5E-10, respectively; weighted means across multiple primary tumor sites) (Figure 6E). In breast cancer patients from the METABRIC cohort[47], the downregulated gene signature was associated with longer recurrence-free (p = 7.1E-4) and overall (p = 0.0055) survival in patients not treated with adjuvant therapy (Figures S6B-C) and shorter recurrence-free and overall survival in patients treated with adjuvant chemo-radiation therapy (p = 0.021 and 0.021, respectively) (Figure 6F-G). The association between the upregulated signature and recurrence-free or overall survival was borderline significant in patients not treated with adjuvant therapy (p = 0.051 and 0.044, respectively; Figures S6D-E) and was not significant in patients treated with adjuvant chemo-radiation therapy (p = 0.7 and 0.39, respectively; Figures S6F-G). These results are consistent with tumors with lower expression of genes downregulated upon addition of nutlin-3a to IR being less proliferative and more resistant to chemo-radiation therapy. Taken together, our findings support a model of p21-mediated downregulation of genes shifting cells into a quiescent state that is resistant to cytotoxic therapy upon addition of nutlin-3a to IR.

Discussion

Revealing roles of network architecture in p53 signaling

The tumor suppressor gene p53 and its transcriptional target p21 are among the most studied genes in biology. However, despite being the subjects of such extensive investigation, how these genes control cell fate decisions that are vital to successful outcomes of anti-cancer therapies are incompletely understood. Given the role of p21-induced cell cycle arrest in treatment resistance, we aimed to uncover how heterogeneous p53 dynamics are propagated to p21 dynamics using combined single cell microscopy and computational modeling. We found that p21 transcription was far better predicted by the change in p53 than absolute p53 level. Three types of three-node network motif capable of fold-change detection have been observed in biology: the IFFL, the nonlinear integral feedback loop, and the logarithmic sensor[48]. Nonlinear integral feedback loops enable fold-change detection in bacterial chemotaxis[49,50], but have not been observed in gene regulation. Logarithmic sensors may play a role in allosteric regulation[51]. Given that the IFFL architecture has previously been shown to regulate transcription of other genes[20,21], we focused our analysis on determining whether expression of p21 transcription is governed in this way. Through constructing and comparing stochastic computational models of PR and IFFL network architectures we determined that p21 transcription is indeed governed by an IFFL. We then proposed that MDM2 binding to p53 is responsible for repression of p21 transcription and successfully validated the need for p53-MDM2 binding to explain p21 transcription dynamics. Pharmacological disruption of the IFFL inhibited and reversed the G1-S transition leading to G0 arrest instead of G2/M checkpoint arrest.

It is important to note that this shift in cell fate is specifically related to the perturbation of the network structure and not just the altered p53 dynamics due to reduction in p53 degradation. Given that UV radiation produces similar p53 dynamics to the IR + nutlin-3a treatment used but different cell fates (predominantly apoptosis rather than cell cycle arrest)[6] in the same cell line, we suggest that transcriptional repression of p21 enabled by MDM2 binding to p53 plays an important role in cell fate specification. UV radiation activates ATR, which inhibits MDM2-dependent degradation of p53, but does not alter MDM2 binding to p53 and, hence, the transcriptional activity of p53[52]. Therefore, UV radiation generates similar p53 dynamics to IR + nutlin-3a, but lower p21 induction. However, this difference in cell fates could alternatively be related to different p53 post-translational modifications in response to the different stimuli.

Beneficial properties of mode of regulation of p21 transcription

Whilst MDM2-dependent transcriptional repression of p53 target genes has been observed previously, the reasons why p53 regulates its target genes in this manner has never been understood. We have demonstrated for the first time how the mechanism of p21 transcription can provide potential advantages to cells over simple positive regulation. Specifically, our analyses indicated that the IFFL architecture facilitates rapid cell cycle arrest and increases p21 noise. These findings, taken in combination with our findings on the influence of p21 protein noise on escape from cell cycle arrest[15], suggest that the IFFL enables a population of cells to rapidly undergo cell cycle arrest following DNA damage and exhibit variability in the timing at which cells will exit cell cycle arrest, and become sensitive to subsequent stresses, reducing the probability of population extinction.

Moreover, our combined experimental and mathematical modelling of the transcriptional dynamics of many p53 target genes found that while a small number of genes are regulated by IFFL, most are instead regulated by PR -- or IFFL with only a mild effect of MDM2 on repression of transcription. Such a difference in the modes of transcriptional regulation would enable cells to decode a multiplexed signal encoded in p53 dynamics. Our proposed model predicts that disrupting the IFFL through inhibiting the binding between p53 and MDM2 would lead to “crosstalk” between the multiple signals encoded in the p53 dynamics, with transcriptional target genes normally regulated by IFFL to parse the change in p53 instead parsing the absolute level of p53, possibly altering cell fates. This property of the p21 IFFL, inferred from bulk transcriptomics data, would be interesting to explore in more detail in future work by performing single cell measurements of multiple different p53 target genes.

Therapeutic implications

Our findings provide important insights for the design of therapeutic strategies based on p53 activation. Due to the role of MDM2 in transcriptional repression of p21, but not apoptosis genes, inhibiting the p53-MDM2 interaction may steer cell fates towards a temporary G0 arrest, rather than apoptosis, protecting cancer cells from cytotoxic therapies targeting proliferating cells. In support of this assertion, p53 induction by nutlin-3a predominantly leads to cell cycle arrest rather than apoptosis in many cell lines[53–55] and protects melanoma cell lines and patient-derived xenografts from mitotic inhibitor-induced DNA damage in a p21-dependent manner[56]. MDM2 antagonists have also been shown to inhibit the senescence associated secretory phenotype and permanent cell cycle arrest[57]. This finding could also be detrimental to successful cancer therapy as induction of tumor cell senescence can increase survival, at least in certain contexts. Given previous work showing that IR-induced senescence results from p53 activation in the G2 phase of the cell cycle[58], our finding that concurrent nutlin-3a and IR administration leads to cells transitioning into the G0 phase of the cell cycle provides a possible explanation for this phenomenon. Alternative explanations include the negative regulation of p53 on mTOR signaling[59]. Our findings that nutlin-3a can steer cells into a therapy-resistant quiescent state caution against the use of MDM2 antagonists concurrently with treatments targeting proliferating cells. Alternative strategies for activating p53 in tumor cells, such as through inhibiting Wip1, may be more likely to cause apoptosis, and hence be superior, to blocking the interaction between p53 and MDM2, which may predominantly result in quiescence.

Our findings indicate that nutlin-3a induced quiescence could instead be exploited in the context of treating p53 mutant tumors by protecting normal tissues from apoptosis and senescence, without affecting cancer cells, thus widening the therapeutic window. Normal cell senescence is responsible for cancer therapy-associated side effects and can promote the aggressiveness of neighboring cancer cells[60], an effect which is inhibited by MDM2 anatagonists[57]. Therefore, steering cells into a temporary G0 arrest, rather than senescence, could be advantageous. This strategy is supported by murine studies demonstrating associations between p21 expression and radioprotection of normal tissue[61–63] and accomplishing radioprotection by pharmacological transient p53 activation[64]. A similar approach has previously been proposed by using CDK4/6 inhibitors to protect normal tissues from radiation through the induction of quiescence[65,66]. However, successful normal tissue protection is highly sensitive to the treatment administration schedule[67]. As such, detailed preclinical studies of the schedule-dependent effects of MDM2 antagonists on normal tissue protection should be performed prior to their clinical evaluation in this context.

Limitations

Our experiments were performed using MCF-7 cells and so the generality of our findings needs to be ascertained in future investigations. Our analysis of TP53 and MDM2 ChIP-seq data from four additional cell lines suggests that different p53 target genes may be IFFL-regulated in different cell lines. Therefore, pharmacologically targeting MDM2 may result in different cell fates in different cell lines, with implications for the previously discussed therapeutic strategies. While the cumulative evidence provided by our study and others indicates that MDM2 antagonists predominantly lead to cell cycle arrest rather than apoptosis, this is not universally true. Concurrent radiation and MDM2 antagonist therapy induced substantial apoptosis and durable tumor regressions in a patient-derived xenograft model of adenoid cystic carcinoma[68]. Note also that MCF-7 rarely undergo apoptosis in response to IR due to caspase-3 deficiency, which could potentially affect the fate of the cells following IR, causing them to undergo cell cycle arrest rather than apoptosis. However, the fact that we observed transcriptional changes consistent with treatment-tolerant persister cells following IR + nutlin-3a suggests that this treatment would be unlikely to predominantly cause apoptosis in a caspase-3 proficient context.

Conclusions

In conclusion, we demonstrated that p21 transcription is governed by an IFFL mediated by MDM2 binding to p53, enabling rapid p21 induction following DNA damage and increasing noise in p21 transcription. Pharmacologically abrogating the IFFL leads to G0 arrest, likely protecting cells against treatments that target proliferating cells. These findings suggest that combining inhibitors of the p53-MDM2 interaction with agents causing double strand breaks may be beneficial in the treatment of p53 mutant, rather than WT, tumors and that alternative p53 activation approaches may be superior in the context treating of p53 WT tumors.

Acknowledgements

We thank members of the Michor and Lahav labs for discussion and comments on the manuscript. This project was supported by funding from the Dana-Farber Cancer Institute Physical Science Oncology Center (NCI U54CA193461 to F.M.), the National Institutes of Health grant R35GM139572 (G.L.) and the Ludwig Center at Harvard (G.L., F.M.). J.A.D. was supported by the Radiation Research Unit at the Cancer Research UK City of London Centre Award [C7893/A28990].

Author contributions

Conceptualization, J.D., J.R., G.L. and F.M.; Methodology, J.D., J.R.; Software, J.D., J.R.; Formal Analysis, J.D.; Investigation, J.D.; Writing – Original Draft, J.D.; Writing – Review & Editing, J.D., J.R., M.T., A.J., G.L. and F.M.; Visualization, J.D.; Supervision, G.L. and F.M.; Funding Acquisition, G.L. and F.M.; Resources, J.R., M.T., A.J. and G.L.

Declaration of interests

F.M. is a cofounder of and has equity in Harbinger Health, has equity in Zephyr AI, and serves as a consultant for Harbinger Health and Zephyr AI. She is also on the board of directors of Exscientia Plc. F.M. declares that none of these relationships are directly or indirectly related to the content of this manuscript.

Figure legends

Figure 1: Transcription of p21 is dependent on the change in p53 rather than its absolute level. (A) p53 protein dynamics, imaged using cyan fluorescent protein, for a representative cell. **(B)** p21 transcription dynamics, imaged using the MS2 system, for the same representative cell as in (A). **(C)** p21 protein dynamics, imaged using mCherry fluorescent protein, for the same representative cell as in (A). **(D)** Smoothed and detrended p53 protein expression for the same cell as in (A). **(E)** Change in p53 protein expression for the same cell as in (D). **(F)** Inferred p21 gene state dynamics for the same cell as in (A) and (B). The gray line shows the p21-MS2 data from (B) and the pink line shows the fit of the hidden Markov model to the data. The y-axis scale indicates the level of the MS2 signal (gray) and additionally the fit of the two-state hidden Markov model (pink), with a value of 0 indicating the "OFF" state and 1 representing the "ON" state. **(G)** Logistic regression model estimating the binary p21 gene state (in (F)) based on the (detrended) absolute p53 expression level (in (D)). **(H)** Logistic regression model estimating the binary p21 gene state (in (F)) based on the change in the (detrended) p53 expression level (in (E). **(I)** Predictive performance of the logistic regression models based on the absolute p53 expression level and change in p53 expression level for all of the cells (all dose levels combined). AUC = area under receiver operating characteristic curve. See also Figure S1.

Figure 2: Transcription of p21 is governed by an incoherent feedforward loop that enables p53 change detection. (A) Diagram of the positive regulation (PR) model of p21 transcriptional regulation. Switching of the *CDKN1A* gene from the "OFF" to the "ON" state depends solely on p53 bound to the promoter. Created with BioRender.com. **(B)** Diagram of the incoherent feedforward loop (IFFL) model of p21 transcriptional regulation. p53 induces expression of a repressor (R) in addition to switching the *CDKN1A* gene from the "OFF" to the "ON" state. Over time, R accumulates and inhibits *CDKN1A* gene activation by binding (either directly or indirectly) to the DNA. Created with BioRender.com. **(C)** Example simulation of p21 transcription dynamics under the PR model. The gray line indicates the p53 dynamics, the black line indicates the measured p21-MS2 dynamics and the blue line indicates the simulated p21-MS2 dynamics. **(D)** Example simulation of p21 transcription dynamics under the IFFL model. The gray line indicates the p53 dynamics, the black line indicates the measured p21-MS2 dynamics and the blue line indicates the simulated p21-MS2 dynamics. **(E)** p21-MS2 autocorrelation function for the same cell as in (C). The black line shows the data and the dark blue line shows the positive regulation model simulation for an example set of parameter values. **(F)** p21-MS2 autocorrelation function for the same cell as in (D). The black line shows the data and the orange line shows the incoherent feedforward loop model simulation for an example set of parameter values. **(G)** p53-p21-MS2 cross-correlation function for the same cell as in (C). The black line shows the data and the dark blue line shows the positive regulation model simulation for an example set of parameter values. **(H)** p53-p21-MS2 cross-correlation function for the same cell as in (D). The black line shows the data and the orange line shows the incoherent feedforward loop model simulation for an example set of parameter values. **(I)** Mean

p21-MS2 autocorrelation function for 10 Gy treated cells for the PR model. **(J)** Mean p53-p21-MS2 cross-correlation function for 10 Gy treated cells for the PR model. **(K)** Mean p21-MS2 autocorrelation function for 10 Gy treated cells for the IFFL model. **(L)** Mean p53-p21-MS2 cross-correlation function for 10 Gy treated cells for the IFFL model. In (I) – (L) the colored lines represent the correlation functions from the simulations that are closest to the correlation functions from the data and the shaded areas represent the 95 percentile confidence intervals of the correlation functions from the simulations. See also Figure S2.

Figure 3: The p53-MDM2 interaction is necessary for transcriptional repression of p21. (A) Mean p21-MS2 autocorrelation function for IR treated cells for the PR model. **(B)** Mean p53 - p21-MS2 cross-correlation function for IR treated cells for the PR model. **(C)** Mean p21-MS2 autocorrelation function for IR + nutlin-3a treated cells for the PR model. **(D)** Mean p53 - p21-MS2 cross-correlation function for IR + nutlin-3a treated cells for the PR model. **(E)** Mean p21-MS2 autocorrelation function for IR treated cells for the IFFL model. **(F)** Mean p53 - p21-MS2 cross-correlation function for IR treated cells for the IFFL model. **(G)** Mean p21-MS2 autocorrelation function for IR + nutlin-3a treated cells for the IFFL model. **(H)** Mean p53 - p21-MS2 cross-correlation function for IR + nutlin-3a treated cells for the IFFL model. In (A) – (H) the colored lines represent the correlation functions from the simulations that are closest to the correlation functions from the data and the shaded areas represent the 95 percentile confidence intervals of the correlation functions from the simulations. **(I)** Predictive performance of logistic regression models of p21 gene state based on p53 expression level and change in p53 expression level for IR treated cells. **(J)** Predictive performance of logistic regression models of p21 gene state based on p53 expression level and change in p53 expression level for IR + nutlin-3a treated cells. AUC = area under receiver operating characteristic curve. See also Figure S3.

Figure 4: The incoherent feedforward loop increases p21 expression response rate and noise and governs a subset of other p53 target genes. (A) Simulated p21 protein dynamics with p21 production governed by PR. **(B)** Simulated p21 protein dynamics with p21 production governed by an IFFL. **(C)** Longitudinal measurements of p21-MS2 noise, as measured by the Fano factor, in cells treated with IR and IR + nutlin-3a. **(D)** Longitudinal measurements of p21-MS2 to p53 protein noise ratio, with noise measured by the Fano factor, in cells treated with IR and IR + nutlin-3a. **(E)** Approach to determining whether the transcription of p53 target genes are governed by PR or IFFL. Under PR the increased expression of a gene upon adding nutlin-3a to IR would be due to the increase in p53 levels alone. Under IFFL the increased expression would be greater than that expected from the increase in p53 levels alone. Created with BioRender.com. **(F)** Positive regulation (dark blue) and incoherent feedforward loop (orange) model simulations for approximate Bayesian computation. The plot shows the relationship between gene expression following IR + nutlin-3a and IR alone for each model and the corresponding measurements for p53 transcriptional target genes (light blue). **(G)** Time course of mRNA expression following IR + nutlin-3a. **(H)** Venn diagram of TP53 and MDM2 ChIP-seq peaks in the LPS141 liposarcoma patient-derived cell line. **(I)** Venn diagram of TP53 and MDM2 ChIP-seq peaks in the LPS853 liposarcoma

patient-derived cell line. **(J)** Distance between TP53, MDM2 and overlapping TP53 and MDM2 (TP53.MDM2) ChIP-seq peaks and transcription start site in LPS141 liposarcoma patient-derived cell line. **(K)** Distance between TP53, MDM2 and overlapping TP53 and MDM2 (TP53.MDM2) ChIP-seq peaks and transcription start site in LPS853 liposarcoma patient-derived cell line. P(IFFL) – posterior probability of IFFL model; IFFL - posterior probability of IFFL model greater than 0.5; TSS Distance – distance between the transcription start site and the closest p53 ChIP-seq peak. See also Figure S4.

Figure 5: Abrogating MDM2-mediated transcriptional repression of p21 prevents and reverses the G1-S transition. (A) Relationship between p21 protein and p53 protein averaged over time points at pseudo-steady state for single cells treated with 10 Gy IR or 10 Gy IR + nutlin-3a. The circular and triangular points designate the first and second components of the mixture distributions, respectively. The contours show the distirbutions of the data. The lines show linear regression fits to the data. **(B)** Slopes and y-intercepts of the regression lines in (A). The dotted line indicates the the value of the slope predicted by the mathematical model. **(C)** Fit of the piecewise linear regression model to p21 protein dynamics following addition of p21 siRNA IR treated cells to infer p21 protein degradation rates for an example cell. **(D)** Distribution of inferred p21 protein degradation rates for all cells. The histogram shows the inferred degradation rates and the line shows a fit of a Gaussian mixture model to the rate distribution. **(E)** Inferred p21 protein production rates for MDM2-repressed and unrepressed p21 production, inferred from the inverse variance weighted mean of the inferred production rates in cells with high and low p21 degradation rates. **(F)** Prediction of p21 protein levels from abrogating the IFFL without altering p53 protein levels in IR treated cells in S phase. The orange points (and error bars) show the predictions (and their standard errors) and the blue contours show the distribution of the data for IR treated cells (same as in (A)). Abrogating the IFFL without altering p53 levels is predicted to increase p21 levels of S phase cells to the levels of those in non-S phase cells. **(G)** Gene set variation analysis of cell cycle phase transcriptional signatures[40]. IR – ionizing radiation; GSVA – gene set variation analysis. See also Figure S5.

Figure 6: Abrogating the p53-MDM2 interaction steers cells into a persister state. (A) RNA-seq differential expression of IR + nutlin-3a versus IR treated MCF-7 cells. **(B)** Transcriptional regulator enrichment analysis for differentially upregulated genes in IR + nutlin-3a versus IR treated MCF-7 cells. **(C)** Transcriptional regulator enrichment analysis for differentially downregulated genes in IR + nutlin-3a versus IR treated MCF-7 cells. **(D)** Gene set variation analysis of IR and IR + nutlin-3a treated MCF-7 cells with cancer persister cell gene sets[55–62]. **(E)** Linear regression model coefficient evaluating the association between radiation response (area under radiation dose-response curve) and GSVA score of genes upregulated and downregulated in IR + nutlin-3a versus IR treated MCF-7 cells, in cell lines from the Cancer Cell Line Encyclopedia[46]. The weighted mean is the inverse variance weighted mean of the coefficients across all primary tumor sites. The size of the points corresponds to the number of cell lines. **(F)** Association between recurrence-free survival and GSVA score of genes downregulated in IR + nutlin-3a versus IR treated MCF-7 cells, in breast cancer patients treated with

chemo-radiation therapy from the METABRIC cohort[47]. **(G)** Association between overall survival and GSVA score of genes downregulated in IR + nutlin-3a versus IR treated MCF-7 cells, in breast cancer patients treated with chemo-radiation therapy from the METABRIC cohort[47]. The p-values in (F) and (G) are from Cox proportional hazards regression models with the signature score, as a continuous variable, as the covariate. OR – odds ratio; GSVA – gene set variation analysis. See also Figure S6.

STAR Methods

Live cell fluorescence microscopy

Live cell fluorescence microscopy, image analysis and quantification of p53 and p21 proteins and p21 transcription following treatment with IR in MCF-7 cells was performed as previously described[18]. In an initial experiment, we treated cells with either 2.5 Gy, 5 Gy or 10 Gy of IR and imaged them for 45 h with a 15 minute temporal resolution (Figures 1, 2, S1A-I, S2A-H, S4D-E). In a second experiment, we treated cells with 10 Gy of IR and imaged them for 15 h with a 2 minute temporal resolution (Figure S1J, S2I-L). In a third experiment to validate the computational model predictions, cells were treated with 10 Gy IR alone or in combination with 10 μM nutlin-3a and imaged for 21 h with either a 15 minute (p53, p21-MS2) or 30 minute (p21) temporal resolution (Figures 3, 4C-D, 5A-F, S3, S4A-C, S5B-D). In these three experiments, 835, 945 and 500 cells, respectively, were successfully segmented and tracked for the duration of the time course. “Outlier” cells with maximum signal intensity greater than 2 interquartile ranges above the 75th quartile, on the $\log_{10}$ scale, were removed. This exclusion criterion led to the removal of 5/835, 2/945 and 1/500 of the cells in the first, second and third experiments, respectively. As the fraction of excluded cells was very small, including these cells would minimally affect the results.

Predictive modeling of p21 gene state based on absolute and change in p53 protein level

Following the “random telegraph” model of gene transcription, we assumed that the p21 gene could be in one of two states: “ON” and “OFF”. We inferred the dynamics of the p21 gene state for each cell by fitting a 2 state hidden Markov model to the p21-MS2 signal for that cell assuming two states and a Gaussian error distribution.

We smoothed the p53 signal using loess smoothing with degree 2 and span 0.1. These parameters were chosen as they were found to successfully remove the spikes in the signal without affecting the p53 oscillations. To remove long-term trends in the p53 signal that were present in IR treated cells, which were deemed likely technical artifacts rather than representing true p53 protein dynamics, we performed b-spline regression with 4 knots on the smoothed p53 signal and subtracted the fitted spline from the smoothed p53 signal. This number of knots was selected as it was found to successfully remove the longer-term trend in the signal while retaining the p53 oscillations.

Delays between the p53 and p21-MS2 signals may occur for biological reasons, such as the time taken for p53 to bind the promoter and recruit the transcriptional machinery, and technical reasons, for example, differences in the maturation times of the different fluorescent reporters. Such delays could bias models. We, therefore, computed the cross-correlation between the p53 and p21-MS2 time course for each cell and shifted the p53 signal to achieve the maximum correlation between the signals. We placed a constraint on the maximum size of the shift of 2.25 h, half the period of p53 oscillations in human cells, to prevent aligning incorrect p53 pulses with bursts of p21 transcription.

We then fit two different univariable logistic regression models to the binary p21 gene state for each cell. For the first model we used the absolute (detrended and shifted) p53 level as the covariate and for the second model we used the change in (detrended and shifted) p53. The predictive performance of the models was assessed using the area under the receiver operating characteristic curve and pairwise comparisons of the predictive performances of the models were performed using paired Wilcoxon tests.

Stochastic modeling of p21 transcription dynamics

As the number of nascent p21 RNA were very small we modeled p21 transcription dynamics as stochastic processes, employing continuous time Markov modeling. We chose to use the p53 data as input into the model rather than explicitly modeling the p53 dynamics for two reasons. Firstly, the dynamics of p53 are complex, being affected by multiple other proteins for which we did not have data. Secondly, it allowed the modeling to be informed by the data, reducing the risk of removing biologically informative dynamics.

In the PR model, the p21 promoter can switch between an "OFF" state (P_{OFF}) and "ON" state (P_{ON}), where the switching to the ON state is dependent on the level of p53. RNA molecules (RNA) are produced at the transcription site only when the promoter is in the "ON" state. The positive regulation model is defined by the following reactions with per capita rates:

Promoter switching off:	$P_{ON} \xrightarrow{k_{OFF}} P_{OFF}$
Promoter switching on:	$P_{OFF} \xrightarrow{k_{ON}p53(t)} P_{ON}$
Production of p21 nascent RNA:	$RNA \xrightarrow{\alpha_{RNA}} RNA + 1$
Release of p21 nascent RNA:	$RNA \xrightarrow{\beta_{RNA}} RNA - 1$

The master equation is given by

$$\frac{\partial P(\boldsymbol{x}, t|\boldsymbol{x}_0, t_0)}{\partial t} = \sum_{j=1}^{M}[a_j(\boldsymbol{x} - \boldsymbol{v}_j)P(\boldsymbol{x} - \boldsymbol{v}_j, t|\boldsymbol{x}_0, t_0) - a_j(\boldsymbol{x})P(\boldsymbol{x}, t|\boldsymbol{x}_0, t_0)]$$

where the state vector for the system is

$$\boldsymbol{x} = \begin{pmatrix} P_{OFF} \\ P_{ON} \\ RNA \end{pmatrix}$$

and the set of reactions is described by the state-transition matrix

$$\boldsymbol{\nu} = \begin{pmatrix} +1 & -1 & 0 & 0 \\ -1 & +1 & 0 & 0 \\ 0 & 0 & +1 & -1 \end{pmatrix}$$

and propensity vector

$$\boldsymbol{a} = \begin{pmatrix} k_{OFF}x[2] \\ k_{ON}p53(t)x[1] \\ \alpha_{RNA}x[2] \\ \beta_{RNA}x[3] \end{pmatrix}$$

The initial state vector is

$$\boldsymbol{x}(0) = \begin{pmatrix} 1 \\ 0 \\ 0 \end{pmatrix}$$

The IFFL model is similar to the PR model, but instead of the promoter switching from the “OFF” to the “ON” state being dependent on the level of p53, it is dependent on the level of p53 above the level of a repressor protein (*R*) whose production is dependent on the level of p53. The model makes the simplifying assumptions of a single step in the production of the repressor (rather than explicitly modeling transcription and translation) and rapid and strong binding of the repressor to p53. The IFFL model is defined by the reactions with the following per capita rates:

Promoter switching off:	$P_{ON} \xrightarrow{k_{OFF}} P_{OFF}$
Promoter switching on:	$P_{OFF} \xrightarrow{k_{ON}(p53(t)-R(t))^{+}} P_{ON}$
Production of p21 nascent RNA:	$RNA \xrightarrow{\alpha_{RNA}} RNA + 1$
Release of p21 nascent RNA:	$RNA \xrightarrow{\beta_{RNA}} RNA - 1$
Production of repressor:	$R \xrightarrow{\alpha_{Repressor}} R + 1$
Degradation of repressor:	$R \xrightarrow{\beta_{Repressor}} R - 1$

The state vector for the system is

$$\boldsymbol{x} = \begin{pmatrix} P_{OFF} \\ P_{ON} \\ RNA \\ R \end{pmatrix}$$

and the set of reactions is described by the state-transition matrix

$$\boldsymbol{v} = \begin{pmatrix} +1 & -1 & 0 & 0 & 0 & 0 \\ -1 & +1 & 0 & 0 & 0 & 0 \\ 0 & 0 & +1 & -1 & 0 & 0 \\ 0 & 0 & 0 & 0 & +1 & -1 \end{pmatrix}$$

and propensity vector

$$\boldsymbol{a} = \begin{pmatrix} k_{OFF}x[2] \\ k_{ON}\left(p53(t) - R(t)\right)^{+}x[1] \\ \alpha_{RNA}x[2] \\ \beta_{RNA}x[3] \\ \alpha_{Repressor}p53(t) \\ \beta_{Repressor}x[4] \end{pmatrix}$$

The initial state vector is

$$\boldsymbol{x}(0) = \begin{pmatrix} 1 \\ 0 \\ 0 \\ p53(0) \end{pmatrix}$$

Simulations were performed using the Gillespie stochastic simulation algorithm. For each run of the simulation, we randomly sampled parameter values from the prior distributions, defined in Supplemental Table 1, and simulated p21 transcription dynamics for the same number of cells as in the dataset that the simulations were being compared to. We performed 5000 simulation runs for each model. To perform the simulations of the time inhomogeneous continuous Markov process we made minor modifications to the ssar R package to increase its speed for our task. This adapted version of the package is available at https://github.com/jamiedean/ssar.

Model comparison by approximate Bayesian computation random forest classification

To select between the two alternative models, we performed model comparison using the approximate Bayesian computation random forest method[76] implemented in the abcrf version 1.9 R package. To formally compare the model simulations to the data we computed the p21 nascent RNA concentration autocorrelation and the cross-correlation between the p53 protein concentration and p21 nascent RNA concentration for all individual cells and took the mean of these functions over all cells, for both the simulations and the data. To account for the maturation time of the p53-tagged fluorescent protein, we advanced the p53 protein concentration time course by 50 minutes relative to the p21 nascent RNA concentration prior to calculating the cross-correlations for the simulations. We did not explicitly model maturation of fluorescent proteins to minimize the number of model parameters. The auto- and cross-correlation functions were chosen as they incorporate the information from the same single cells over time[77], unlike the moments of distributions over all of the cells at single timepoints. The correlation function values at the first five peaks and troughs of the mean auto-correlation function and the five peaks and troughs closest to a lag of 0 of the mean cross-correlation function were chosen as the summary statistics for Bayesian model comparison. The random forest model used 3000 trees (a number chosen because the out-of-bag performance had converged with this number of trees) and added linear discriminant analysis to the summary statistics. We only performed model comparison and did not perform parameter inference as this requires a much larger number of parameter sets, and therefore simulations, which would take several months with our available hardware.

Delay differential equation models of p21 dynamics

Delay differential equation models of p53 and p21 dynamics were developed to perform a mathematically controlled comparison of the effect of the IFFL on the p21 induction rate. The functional form of our model was inspired by two previous models, one of p53 dynamics, incorporating activation of p53 by phosphorylated ATM (pATM) and negative regulation by the p53 transcriptional target genes MDM2 and Wip1[78], and another of p21 dynamics, incorporating a bistable switch between p21 and CDK2[15]. We added two alternative p21 protein compartments, with p21 production governed either by PR ($p21_{PR}$) or IFFL ($p21_{IFFL}$):

$$\frac{d[p53_{inactive}]}{dt} = \beta_p - \alpha_{mpi}[MDM2][p53_{inactive}] - \beta_{sp}[p53_{inactive}]\left(\frac{[pATM]^{n_s}}{[pATM]^{n_s} + T_s^{n_s}}\right) + \alpha_{wpa}[Wip1][p53_{active}] - \alpha_{pi}[p53_{inactive}]$$

$$\frac{d[p53_{active}]}{dt} = \beta_{sp}[p53_{inactive}]\left(\frac{[pATM]^{n_s}}{[pATM]^{n_s} + T_s^{n_s}}\right) - \alpha_{wpa}[Wip1][p53_{active}] - \alpha_{mpa}[p53_{active}]$$

$$\frac{d[MDM2]}{dt} = \beta_m[p53_{active}(t - \tau_m)] + \beta_{mi} - \alpha_{sm}[pATM][MDM2] - \alpha_m[MDM2]$$

$$\frac{d[Wip1]}{dt} = \beta_w[p53_{active}(t - \tau_w)] - \alpha_w[Wip1]$$

$$\frac{d[pATM]}{dt} = \beta_s - \alpha_s[pATM] - \alpha_{ws}[pATM]\left(\frac{[Wip1]^{n_w}}{[Wip1]^{n_s} + T_w^{n_w}}\right)$$

$$\frac{d[p21_{PR}]}{dt} = \beta_c^{PR}[p53_{active}(t-\tau_c)] - \alpha_c[p21_{PR}] - \lambda\beta_3\left(\frac{CDK2_{activity,PR}^{n_2}}{CDK2_{activity,PR}^{n_2} + K_2^{n_2}}\right)$$

where $CDK2_{activity,PR} = \alpha_3\left(\frac{K_1^{n_1}}{\log(p21_{PR}+1)^{n_1} + K_1^{n_1}}\right)$

$$\frac{d[p21_{IFFL}]}{dt} = \beta_c^{IFFL}([p53_{active}(t-\tau_c)] - [MDM2(t-\tau_c)])^+ - \alpha_c[p21_{IFFL}] - \lambda\beta_3\left(\frac{CDK2_{activity,IFFL}^{n_2}}{CDK2_{activity,IFFL}^{n_2} + K_2^{n_2}}\right)$$

where $CDK2_{activity,IFFL} = \alpha_3\left(\frac{K_1^{n_1}}{\log(p21_{IFFL}+1)^{n_1} + K_1^{n_1}}\right)$

The model parameter values and initial conditions used are given in Supplemental Table 2. We chose the same parameter values and initial conditions as those used in the original publications as these had previously been shown to reproduce the relevant experimental measurements, with the following exceptions: (i) we selected the value for the p21 production rate under positive regulation (β_c^{PR}) and scaling of the CDK2-dependent p21 degradation (λ) to produce similar p21 dynamics as observed in our data; (ii) we selected the p21 production rate under incoherent feedforward loop regulation (β_c^{IFFL}) to produce a pseudo-steady state level of p21 matching that under positive regulation; (iii) we selected the time delay in p21 production (τ_c) to match that of MDM2. The model was implemented in Julia using the DifferentialEquations package. Note that neither the details of the part of the model that produces the p53 oscillations nor govern p21 degradation affect the relationship between IFFL regulation of p21 production and increased response rate. Alternative mathematical models of p53 dynamics and p21 degradation, demonstrate the same relationship between the mode of p21 regulation and response rate (confirmed when constructing this model).

Inferring the mode of transcriptional regulation of p53 target genes

Time course RNA-sequencing data and p53 protein levels of MCF-7 cells treated with IR and IR + nutlin-3a were obtained from a previous study[35]. The p53 proteins were smoothed using a smoothing spline with 12 knots, a number selected based on successfully capturing the known patterns of p53 dynamics following IR and IR + nutlin-3a.

The dynamics of p53 transcriptional target gene mRNA expression, *M*, were modelled using ordinary differential equation models with transcription governed by either PR or IFFL:

$$\frac{dM_{IR}}{dt} = \frac{\alpha . p53_{IR}(t)}{p53_{IR}(t) + K} - \beta . M_{IR}$$

$$\frac{dM_{IR+nutlin,PR}}{dt} = \frac{\alpha . p53_{IR+nutlin}(t)}{p53_{IR+nutlin}(t) + K} - \beta . M_{IR+nutlin,PR}$$

$$\frac{dM_{IR+nutlin,IFFL}}{dt} = \frac{(\alpha + \gamma(t)) . p53_{IR+nutlin}(t)}{p53_{IR+nutlin}(t) + K} - \beta . M_{IR+nutlin,IFFL}$$

$$\gamma(t) = \begin{cases} 0 & t \leq 3 \\ \gamma & t > 3 \end{cases}$$

where α is the transcription rate, β is the degradation rate, K is the Michaelis-Menten constant, and γ is the increase in transcription rate due to inhibition of transcriptional repression in the presence of nutlin-3a. The time dependence of γ is due to nutlin-3a being administered 3 h after IR administration.

mRNA expression dynamics were simulated under both models for 10,000 different combinations of parameter values, with parameters sampled from the prior distributions defined in Supplemental Table 3. Model comparison was performed using approximate Bayesian computation random forest method[76] implemented in the abcrf version 1.9 R package. The mRNA levels at each timepoint under both treatment conditions were used as the summary statistics. For the data, the mean values across the two replicates were used. The random forest model used 3000 trees (a number selected because the out-of-bag performance had converged with this number of trees) and added linear discriminant analysis to the summary statistics.

ChIP-seq data analysis

TP53 and MDM2 ChIP-seq data of four cell lines were obtained from a previous study[36]. Overlaps between TP53 and MDM2 peaks and distances from the centers of TP53 peaks to transcription start sites were computed using the ChIPpeakAnno version 3.34.1 R package, with genes annotated using the TxDb.Hsapiens.UCSC.hg38.knownGene version 3.17.0 R package. The analysis of distances between TP53 peaks and transcription start sites was not performed for the HCT116 and U2OS cell lines as the number of overlapping TP53 and MDM2 peaks was too small (3 and 4 overlapping TP53 and MDM2 peaks, respectively) to perform a meaningful statistical analysis.

Theoretical modeling for inference of p21 production and degradation rates

To infer p21 production and degradation rates from timelapse microscopy data, we begin by assuming that p21 protein concentration, $[p21]$, is described by the ordinary differential equation

$$\frac{d[p21]}{dt} = \alpha \frac{[p53]}{[p53]+K} - \beta[p21] \qquad (1)$$

where α is rate of production of the p21 protein, K is the Michaelis-Menten constant and β is the degradation rate of the p21 protein. At pseudo-steady state, $\frac{d[p21]}{dt} \approx 0$, and equation (1) can be rearranged to give

$$[p21] \approx \frac{\alpha}{\beta} \frac{[p53]}{[p53]+K} \qquad (2)$$

If $[p53] \gg K$, then

$$[p21] \approx \frac{\alpha}{\beta} \qquad (3)$$

Therefore, given the assumptions of this model, for sufficiently high levels of p53, plotting $[p21]$ against $[\mathrm{p53}]$ would give rise to a straight line with slope of 0 and y-intercept of $\frac{\alpha}{\beta}$. If this theoretical insight is correct, and assuming that p21 degradation rate is unaffected by nutlin-3a, this argument would enable the relative difference in the p21 production rate between cells treated with IR alone and IR + nutlin-3a to be inferred. Measuring the degradation rate of p21 (method described below) enables the absolute p21 production rates in the absence and presence of nutlin-3a to be inferred by

$$\alpha \approx \beta[p21] \qquad (4)$$

As p21 has two different degradation rates: rapid degradation in S phase of the cell cycle and slow degradation in the remainder of the cell cycle[37], Gaussian mixture models with 2 components were fit to the [*p21*] data for each treatment condition. For each treatment condition, the p21 production rate was inferred separately for each of the two mixture components and the inverse variance weighted mean was used to combine these estimates into a single production rate estimate.

To predict the effect of abrogating MDM2-mediated transcriptional repression without affecting p53 degradation, and therefore p53 levels, in S phase cells (rapid p21 degradation), we multiplied the p21 levels of IR treated cells in the mixture component with lower p21 levels by the ratio of production rates inferred for IR + nutlin-3a and IR treated cells (Figure 5F). To predict the effect of abrogating MDM2-mediated p53 degradation without affecting transcriptional repression, we added the difference in the mean p53 levels between IR + nutlin-3a and IR treated cells to the p53 levels of IR treated cells in the mixture component with lower p21 levels (Figure S5B). In both cases we computed standard errors by propagating errors in the rate and protein steady state level estimates.

Measurement and inference of p21 degradation rates

MCF-7 cells were treated with IR and then imaged with a 15 minute temporal resolution with 40 nM siRNA targeting either p21 alone or p53 and p21 at 20 h. Piecewise linear regression models were fit to the log-transformed p21 protein signal versus time from 27.5 h (to allow time sufficient time for p21 protein production to be inhibited) for each cell individually using the dpseg version 0.1.1 R package. The slopes of the first two lines were taken to be the low and high degradation rates for each cell. A Gaussian mixture model with 2 components was fit to the distribution of inferred degradation rates (combining cells from both datasets as there was the degradation dynamics were the same under both conditions) using the mclust version 6.0.1 R package.

RNA-sequencing data analysis

Raw RNA-seq time course data of MCF-7 cells sequenced from 3 h to 12 h in 1 h intervals following treatment with IR and IR + nutlin-3a[35] were downloaded from the Gene Expression Omnibus (GSE100099). Expression of transcripts was quantified using Salmon version 1.1.0[79] with GENCODE release 33[80] Homo sapiens GRCh38 for the reference transcriptome annotation. Differential expression analysis was performed to test for differences in gene expression over time between treatments using the likelihood ratio test, with expression ~ time + replicate + treatment + treatment:time as the full model and expression ~ time + replicate + treatment as the reduced model, in the DESeq2 version 1.40.2 R package.

Transcription factor enrichment analysis

Transcription factor enrichment analysis was performed using the TFEA.ChIP version 1.20.0 R package[81] with the ReMap2022+EnsTSS+CellTypeEnh.Rdata database accessed from https://github.com/LauraPS1/TFEA.ChIP_downloads/tree/master/R%20Databases. Over-representation analysis of transcriptional regulators for significantly upregulated and downregulated genes was performed. Upregulated and downregulated genes were defined as those with a differential expression adjusted p-value less than 0.05 and a positive or negative estimates of differences in gene expression over time, respectively. Genes with a differential expression adjusted p-value greater than 0.5 were selected as control genes.

Transcriptional signatures

Transcriptional signature scores were calculated with gene set variance analysis, implemented in the GSVA version 1.48.3 R package. Cell cycle phase[40], nuclear size[82] and persister cell signatures[55–62] were obtained from the referenced studies.

Gene expression signatures were created for genes significantly upregulated and downregulated in IR + nutlin versus IR treated cells with an adjusted p-value of less than 0.05 and effect size of magnitude greater than 0.5. The associations between the upregulated and downregulated gene expression signatures and cell line radiation response were measured by fitting linear regression models with area under the radiation dose response curve as the outcome variable and the gene set variance analysis signature scores as the covariate, using data from the RadioGx version 4.2.0 R package[46]. Separate regression models were fit for cell lines from different primary disease sites, for disease sites with at least 10 cell lines, and an inverse variance weighted mean coefficient across all of the primary disease sites calculated (Figure 6E).

The associations between the upregulated and downregulated gene expression signatures and breast cancer patient recurrence-free and overall survival were measured by fitting Cox proportional hazards regression models with the gene set variance analysis signature scores as the covariates, using data from the METABRIC cohort[47] (Figures 6F-G and S6B-G). Patients treated with hormone therapy (n = 1216) were excluded as hormone therapy could potentially confound inference of cytotoxic therapy response, leaving 311 patients receiving no adjuvant therapy and 173 patients treated with radiation and chemotherapy.

Materials availability

This study did not generate new unique reagents.

Data and code availability

Data and code are available at https://github.com/jamiedean/p21-iffl-regulation.

References

1. Cohen, A.A., Geva-Zatorsky, N., Eden, E., Frenkel-Morgenstern, M., Issaeva, I., Sigal, A., Milo, R., Cohen-Saidon, C., Liron, Y., Kam, Z., et al. (2008). Dynamic proteomics of individual cancer cells in response to a drug. Science *322*, 1511–1516. https://doi.org/10.1126/science.116016.

2. Sharma, S.V., Lee, D.Y., Li, B., Quinlan, M.P., Takahashi, F., Maheswaran, S., McDermott, U., Azizian, N., Zou, L., Fischbach, M.A., et al. (2010). A Chromatin-Mediated Reversible Drug-Tolerant State in Cancer Cell Subpopulations. Cell *141*, 69–80. https://doi.org/10.1016/j.cell.2010.02.027.

3. Roesch, A., Fukunaga-Kalabis, M., Schmidt, E.C., Zabierowski, S.E., Brafford, P.A., Vultur, A., Basu, D., Gimotty, P., Vogt, T., and Herlyn, M. (2010). A Temporarily Distinct Subpopulation of Slow-Cycling Melanoma Cells Is Required for Continuous Tumor Growth. Cell *141*, 583–594. https://doi.org/10.1016/j.cell.2010.04.020.

4. Liau, B.B., Sievers, C., Donohue, L.K., Gillespie, S.M., Flavahan, W.A., Miller, T.E., Venteicher, A.S., Hebert, C.H., Carey, C.D., Rodig, S.J., et al. (2017). Adaptive Chromatin Remodeling Drives Glioblastoma Stem Cell Plasticity and Drug Tolerance. Cell Stem Cell *20*, 233-246.e7. https://doi.org/10.1016/j.stem.2016.11.003.

5. Ryl, T., Kuchen, E.E., Bell, E., Shao, C., Flórez, A.F., Mönke, G., Gogolin, S., Friedrich, M., Lamprecht, F., Westermann, F., et al. (2017). Cell-Cycle Position of Single MYC-Driven Cancer Cells Dictates Their Susceptibility to a Chemotherapeutic Drug. Cell Syst. *5*, 237-250.e8. https://doi.org/10.1016/j.cels.2017.07.005.

6. Purvis, J., Loewer, A., and Lahav, G. (2012). p53 Dynamics Control Cell Fate. Science *336*, 13–16. https://doi.org/10.1126/science.1218351.

7. Paek, A.L., Liu, J.C., Forrester, W.C., Lahav, G., Paek, A.L., Liu, J.C., Loewer, A., Forrester, W.C., and Lahav, G. (2016). Cell-to-Cell Variation in p53 Dynamics Leads to Fractional Killing. Cell *165*, 631–642. https://doi.org/10.1016/j.cell.2016.03.025.

8. Xiong, Y., Hannon, G.J., Zhang, H., Casso, D., Kobayashi, R., and Beach, D. (1993). P21 is a universal inhibitor of cyclin kinases. Nature *366*, 701–704. https://doi.org/10.1038/366701a0.

9. Wade Harper, J., Adami, G.R., Wei, N., Keyomarsi, K., and Elledge, S.J. (1993). The p21 Cdk-interacting protein Cip1 is a potent inhibitor of G1 cyclin-dependent kinases. Cell *75*, 805–816. https://doi.org/10.1016/0092-8674(93)90499-G.

10. El-Deiry, W.S., Tokino, T., Velculescu, V.E., Levy, D.B., Parsons, R., Trent, J.M., Lin, D., Mercer, W.E., Kinzler, K.W., and Vogelstein, B. (1993). WAF1, a Potential Mediator of p53 Tumor Suppression. Cell *75*, 817–825. https://doi.org/10.1016/0092-8674(93)90500-p.

11. Waldman, T., Kinzler, K.W., and Vogelstein, B. (1995). p21 Is Necessary for the p53-mediated G1 Arrest in Human Cancer Cells. Cancer Res. *55*, 5187–5190.

12. Bunz, F., Dutriaux, A., Lengauer, C., Waldman, T., Zhou, S., Brown, J.P., Sedivy, J.M., Kinzler, K.W., and Vogelstein, B. (1998). Requirement for p53 and p21 to sustain G2 arrest after DNA damage. Science *282*, 1497–1501. https://doi.org/10.1126/science.282.5393.1497.

13. Spencer, S.L., Cappell, S.D., Tsai, F.C., Overton, K.W., Wang, C.L., and Meyer, T. (2013). The proliferation-quiescence decision is controlled by a bifurcation in CDK2 activity at mitotic exit. Cell *155*, 369–383. https://doi.org/10.1016/j.cell.2013.08.062.

14. Wesley Overton, K., Spencer, S.L., Noderer, W.L., Meyer, T., and Wang, C.L. (2014). Basal p21 controls population heterogeneity in cycling and quiescent cell cycle states. Proc. Natl. Acad. Sci. U. S. A. *111*, E4386–E4393. https://doi.org/10.1073/pnas.1409797111.

15. Reyes, J., Chen, J.Y., Stewart-Ornstein, J., Karhohs, K.W., Mock, C.S., and Lahav, G. (2018). Fluctuations in p53 Signaling Allow Escape from Cell-Cycle Arrest. Mol. Cell *71*, 581-591.e5. https://doi.org/10.1016/j.molcel.2018.06.031.

16. Overton, K.W., Spencer, S.L., Noderer, W.L., Meyer, T., and Wang, C.L. (2014). Basal p21 controls population heterogeneity in cycling and quiescent cell cycle states. Proc. Natl. Acad. Sci. *111*, E4386–E4393. https://doi.org/10.1073/pnas.1409797111.

17. Hsu, C.-H., Altschuler, S.J., and Wu, L.F. (2019). Patterns of Early p21 Dynamics Determine Proliferation-Senescence Cell Fate after Chemotherapy. Cell *178*, 361-373.E12. https://doi.org/10.1016/j.cell.2019.05.041.

18. Hafner, A., Reyes, J., Stewart-Ornstein, J., Tsabar, M., Jambhekar, A., and Lahav, G. (2020). Quantifying the Central Dogma in the p53 Pathway in Live Single Cells. Cell Syst. *10*, 495-505.e4. https://doi.org/10.1016/j.cels.2020.05.001.

19. Lahav, G., Rosenfeld, N., Sigal, A., Geva-zatorsky, N., Levine, A.J., Elowitz, M.B., and Alon, U. (2004). Dynamics of the p53-Mdm2 feedback loop in individual cells. Nat. Genet. *36*, 147–150. https://doi.org/10.1038/ng1293.

20. Lee, R.E.C., Walker, S.R., Savery, K., Frank, D.A., and Gaudet, S. (2014). Fold change of nuclear NF-κB determines TNF-induced transcription in single cells. Mol. Cell *53*, 867–879. https://doi.org/10.1016/j.molcel.2014.01.026.

21. Frick, C.L., Yarka, C., Nunns, H., and Goentoro, L. (2017). Sensing relative signal in the Tgf-β/Smad pathway. Proc. Natl. Acad. Sci. U. S. A. *114*, E2975–E2982. https://doi.org/10.1073/pnas.1611428114.

22. Oliner, J.D., Pietenpol, J.A., Thiagalingam, S., Gyuris, J., Kinzler, K.W., and Vogelstein, B. (1993). Oncoprotein MDM2 conceals the activation domain of tumour suppressor p53. Nature *362*, 857–860. https://doi.org/10.1038/362857a0.

23. Minsky, N., and Oren, M. (2004). The RING domain of Mdm2 mediates histone ubiquitylation and transcriptional repression. Mol. Cell *16*, 631–639. https://doi.org/10.1016/j.molcel.2004.10.016.

24. White, D.E., Talbott, K.E., Arva, N.C., and Bargonetti, J. (2006). Mouse double minute 2 associates with chromatin in the presence of p53 and is released to facilitate activation of transcription. Cancer Res. *66*, 3463–3470. https://doi.org/10.1158/0008-5472.CAN-05-1381.

25. Tang, Y., Zhao, W., Chen, Y., Zhao, Y., and Gu, W. (2008). Acetylation Is Indispensable for p53 Activation. Cell *133*, 612–626. https://doi.org/10.1016/j.cell.2008.03.025.

26. Momand, J., Zambetti, G.P., Olson, D.C., George, D., and Levine, A.J. (1992). The mdm-2 oncogene product forms a complex with the p53 protein and inhibits p53-mediated transactivation. Cell *69*, 1237–1245. https://doi.org/10.1016/0092-8674(92)90644-R.

27. Thut, C.J., Goodrich, J.A., and Tjian, R. (1997). Repression of p53-mediated transcription by MDM2: A dual mechanism. Genes Dev. *11*, 1974–1986. https://doi.org/10.1101/gad.11.15.1974.

28. Vassilev, L.T., Vu, B.T., Graves, B., Carvajal, D., Podlaski, F., Filipovic, Z., Kong, N., Kammlott, U., Lukacs, C., Klein, C., et al. (2004). In Vivo Activation of the p53 Pathway by Small-

Molecule Antagonists of MDM2. Science *303*, 844–848. https://doi.org/10.1126/science.1092472.

29. Mangan, S., and Alon, U. (2003). Structure and function of the feed-forward loop network motif. Proc. Natl. Acad. Sci. U. S. A. *100*, 11980–11985. https://doi.org/10.1073/pnas.2133841100.

30. Mangan, S., Itzkovitz, S., Zaslaver, A., and Alon, U. (2006). The incoherent feed-forward loop accelerates the response-time of the gal system of Escherichia coli. J. Mol. Biol. *356*, 1073–1081. https://doi.org/10.1016/j.jmb.2005.12.003.

31. El-Samad, H. (2021). Biological feedback control—Respect the loops. Cell Syst. *12*, 477–487. https://doi.org/10.1016/j.cels.2021.05.004.

32. Kittisopikul, M., and Süel, G.M. (2010). Biological role of noise encoded in a genetic network motif. Proc. Natl. Acad. Sci. U. S. A. *107*, 13300–13305. https://doi.org/10.1073/pnas.1003975107.

33. Ronde, W.D., and Wolde, P.R. (2014). Multiplexing oscillatory biochemical signals. Phys. Biol. *11*, 026004. https://doi.org/10.1088/1478-3975/11/2/026004.

34. Kaplan, S., Bren, A., Dekel, E., and Alon, U. (2008). The incoherent feed-forward loop can generate non-monotonic input functions for genes. Mol. Syst. Biol. *4*, 203. https://doi.org/10.1038/msb.2008.43.

35. Hafner, A., Stewart-Ornstein, J., Purvis, J.E., Forrester, W.C., Bulyk, M.L., and Lahav, G. (2017). P53 pulses lead to distinct patterns of gene expression albeit similar DNA-binding dynamics. Nat. Struct. Mol. Biol. *24*, 840–847. https://doi.org/10.1038/nsmb.3452.

36. Bevill, S.M., Casaní-Galdón, S., El Farran, C.A., Cytrynbaum, E.G., Macias, K.A., Oldeman, S.E., Oliveira, K.J., Moore, M.M., Hegazi, E., Adriaens, C., et al. (2023). Impact of supraphysiologic MDM2 expression on chromatin networks and therapeutic responses in sarcoma. Cell Genomics *3*, 100321. https://doi.org/10.1016/j.xgen.2023.100321.

37. Kim, Y., Starostina, N.G., and Kipreos, E.T. (2008). The CRL4Cdt2 ubiquitin ligase targets the degradation of p21Cip1 to control replication licensing. Genes Dev. *22*, 2507–2519. https://doi.org/10.1101/gad.1703708.

38. Barr, A.R., Cooper, S., Heldt, F.S., Butera, F., Stoy, H., Mansfeld, J., Novák, B., and Bakal, C. (2017). DNA damage during S-phase mediates the proliferation-quiescence decision in the subsequent G1 via p21 expression. Nat. Commun. *8*, 14728. https://doi.org/10.1038/ncomms14728.

39. Heldt, F.S., Barr, A.R., Cooper, S., Bakal, C., and Novák, B. (2018). A comprehensive model for the proliferation–quiescence decision in response to endogenous DNA damage in

human cells. Proc. Natl. Acad. Sci. *115*, 2532–2537. https://doi.org/10.1073/pnas.1715345115.

40. Xue, J.Y., Zhao, Y., Aronowitz, J., Mai, T.T., Vides, A., Qeriqi, B., Kim, D., Li, C., De Stanchina, E., Mazutis, L., et al. (2020). Rapid non-uniform adaptation to conformation-specific KRAS(G12C) inhibition. Nature *577*, 421–425. https://doi.org/10.1038/s41586-019-1884-x.

41. Litovchick, L., Sadasivam, S., Florens, L., Zhu, X., Swanson, S.K., Velmurugan, S., Chen, R., Washburn, M.P., Liu, X.S., and DeCaprio, J.A. (2007). Evolutionarily Conserved Multisubunit RBL2/p130 and E2F4 Protein Complex Represses Human Cell Cycle-Dependent Genes in Quiescence. Mol. Cell *26*, 539–551. https://doi.org/10.1016/j.molcel.2007.04.015.

42. Engeland, K. (2018). Cell cycle arrest through indirect transcriptional repression by p53: I have a DREAM. Cell Death Differ. *25*, 114–132. https://doi.org/10.1038/cdd.2017.172.

43. Santoro, A., Vlachou, T., Luzi, L., Melloni, G., Mazzarella, L., D'Elia, E., Aobuli, X., Pasi, C.E., Reavie, L., Bonetti, P., et al. (2019). p53 Loss in Breast Cancer Leads to Myc Activation, Increased Cell Plasticity, and Expression of a Mitotic Signature with Prognostic Value. Cell Rep. *26*, 624-638.e8. https://doi.org/10.1016/j.celrep.2018.12.071.

44. Sarosiek, K.A., Fraser, C., Muthalagu, N., Bhola, P.D., Chang, W., McBrayer, S.K., Cantlon, A., Fisch, S., Golomb-Mello, G., Ryan, J.A., et al. (2017). Developmental Regulation of Mitochondrial Apoptosis by c-Myc Governs Age- and Tissue-Specific Sensitivity to Cancer Therapeutics. Cancer Cell *31*, 142–156. https://doi.org/10.1016/j.ccell.2016.11.011.

45. Topham, C., Tighe, A., Ly, P., Bennett, A., Sloss, O., Nelson, L., Ridgway, R.A., Huels, D., Littler, S., Schandl, C., et al. (2015). MYC Is a Major Determinant of Mitotic Cell Fate. Cancer Cell *28*, 129–140. https://doi.org/10.1016/j.ccell.2015.06.001.

46. Manem, V.S.K., Lambie, M., Smith, I., Smirnov, P., Kofia, V., Freeman, M., Koritzinsky, M., Abazeed, M.E., Haibe-Kains, B., and Bratman, S.V. (2019). Modeling cellular response in large-scale radiogenomic databases to advance precision radiotherapy. Cancer Res. *79*, 6227–6237. https://doi.org/10.1158/0008-5472.CAN-19-0179.

47. Pereira, B., Chin, S.-F., Rueda, O.M., Vollan, H.-K.M., Provenzano, E., Bardwell, H.A., Pugh, M., Jones, L., Russell, R., Sammut, S.-J., et al. (2016). The somatic mutation profiles of 2,433 breast cancers refine their genomic and transcriptomic landscapes. Nat. Commun. *7*, 11479. https://doi.org/10.1038/ncomms11479.

48. Adler, M., and Alon, U. (2018). Fold-change detection in biological systems. Curr. Opin. Syst. Biol. *8*, 81–89. https://doi.org/10.1016/j.coisb.2017.12.005.

49. Lazova, M.D., Ahmed, T., Bellomo, D., Stocker, R., and Shimizu, T.S. (2011). Response rescaling in bacterial chemotaxis. Proc. Natl. Acad. Sci. U. S. A. *108*, 13870–13875. https://doi.org/10.1073/pnas.1108608108.

50. Kojadinovic, M., Armitage, J.P., Tindall, M.J., and Wadhams, G.H. (2013). Response kinetics in the complex chemotaxis signalling pathway of Rhodobacter sphaeroides. J. R. Soc. Interface *10*, 20121001. https://doi.org/10.1098/rsif.2012.1001.

51. Olsman, N., and Goentoro, L. (2016). Allosteric proteins as logarithmic sensors. Proc. Natl. Acad. Sci. U. S. A. *113*, E4423–E4430. https://doi.org/10.1073/pnas.1601791113.

52. Heltberg, M.L., Chen, S. hong, Jiménez, A., Jambhekar, A., Jensen, M.H., and Lahav, G. (2019). Inferring Leading Interactions in the p53/Mdm2/Mdmx Circuit through Live-Cell Imaging and Modeling. Cell Syst. *9*, 548-558.e5. https://doi.org/10.1016/j.cels.2019.10.010.

53. Henry, R.E., Andrysik, Z., París, R., Galbraith, M.D., and Espinosa, J.M. (2012). A DR4:tBID axis drives the p53 apoptotic response by promoting oligomerization of poised BAX. EMBO J. *31*, 1266–1278. https://doi.org/10.1038/emboj.2011.498.

54. Sullivan, K.D., Padilla-Just, N., Henry, R.E., Porter, C.C., Kim, J., Tentler, J.J., Eckhardt, S.G., Tan, A.C., DeGregori, J., and Espinosa, J.M. (2012). ATM and MET kinases are synthetic lethal with nongenotoxic activation of p53. Nat. Chem. Biol. *8*, 646–654. https://doi.org/10.1038/nchembio.965.

55. Allen, M.A., Andrysik, Z., Dengler, V.L., Mellert, H.S., Guarnieri, A., Freeman, J.A., Sullivan, K.D., Galbraith, M.D., Luo, X., Lee Kraus, W., et al. (2014). Global analysis of p53-regulated transcription identifies its direct targets and unexpected regulatory mechanisms. eLife *3*, e02200. https://doi.org/10.7554/eLife.02200.001.

56. Vilgelm, A.E., Cobb, P., Malikayil, K., Flaherty, D., Andrew Johnson, C., Raman, D., Saleh, N., Higgins, B., Vara, B.A., Johnston, J.N., et al. (2017). MDM2 Antagonists Counteract Drug-Induced DNA Damage. EBioMedicine *24*, 43–55. https://doi.org/10.1016/j.ebiom.2017.09.016.

57. Wiley, C.D., Schaum, N., Alimirah, F., Lopez-Dominguez, J.A., Orjalo, A.V., Scott, G., Desprez, P.Y., Benz, C., Davalos, A.R., and Campisi, J. (2018). Small-molecule MDM2 antagonists attenuate the senescence-associated secretory phenotype. Sci. Rep. *8*, 2410. https://doi.org/10.1038/s41598-018-20000-4.

58. Krenning, L., Feringa, F.M., Shaltiel, I.A., vandenBerg, J., and Medema, R.H. (2014). Transient activation of p53 in G2 phase is sufficient to induce senescence. Mol. Cell *55*, 59–72. https://doi.org/10.1016/j.molcel.2014.05.007.

59. Budanov, A.V., and Karin, M. (2008). p53 Target Genes Sestrin1 and Sestrin2 Connect Genotoxic Stress and mTOR Signaling. Cell *134*, 451–460. https://doi.org/10.1016/j.cell.2008.06.028.

60. Demaria, M., O'Leary, M.N., Chang, J., Shao, L., Liu, S., Alimirah, F., Koenig, K., Le, C., Mitin, N., Deal, A.M., et al. (2017). Cellular senescence promotes adverse effects of chemotherapy

and cancer relapse. Cancer Discov. *7*, 165–176. https://doi.org/10.1158/2159-8290.CD-16-0241.

61. Wang, Y.A., Elson, A., and Leder, P. (1997). Loss of p21 increases sensitivity to ionizing radiation and delays the onset of lymphoma in atm-deficient mice. Proc. Natl. Acad. Sci. *94*, 14590–14595. https://doi.org/10.1073/pnas.94.26.14590.

62. Sullivan, J.M., Jeffords, L.B., Lee, C.-L., Rodrigues, R., Ma, Y., and Kirsch, D.G. (2012). p21 Protects “Super p53” Mice from the Radiation-Induced Gastrointestinal Syndrome. Radiat. Res. *177*, 307–310. https://doi.org/10.1667/RR2545.1.

63. Nag, D., Bhanja, P., Riha, R., Sanchez-Guerrero, G., Kimler, B.F., Tsue, T.T., Lominska, C., and Saha, S. (2019). Auranofin Protects Intestine against Radiation Injury by Modulating p53/p21 Pathway and Radiosensitizes Human Colon Tumor. Clin. Cancer Res. *25*, 4791–4807. https://doi.org/10.1158/1078-0432.CCR-18-2751.

64. Pant, V., Xiong, S., Wasylishen, A.R., Larsson, C.A., Aryal, N.K., Chau, G., Tailor, R.C., and Lozano, G. (2019). Transient enhancement of p53 activity protects from radiation-induced gastrointestinal toxicity. Proc. Natl. Acad. Sci. U. S. A. *116*, 17429–17437. https://doi.org/10.1073/pnas.1909550116.

65. Johnson, S.M., Torrice, C.D., Bell, J.F., Monahan, K.B., Jiang, Q., Wang, Y., Ramsey, M.R., Jin, J., Wong, K.-K., Su, L., et al. (2010). Mitigation of hematologic radiation toxicity in mice through pharmacological quiescence induced by CDK4/6 inhibition. J. Clin. Invest. *120*, 2528–2536. https://doi.org/10.1172/JCI41402.

66. Wei, L., Leibowitz, B.J., Wang, X., Epperly, M., Greenberger, J., Zhang, L., and Yu, J. (2016). Inhibition of CDK4/6 protects against radiation-induced intestinal injury in mice. J. Clin. Invest. *126*, 4076–4087. https://doi.org/10.1172/JCI88410.

67. Lee, C.-L., Oh, P., Xu, E.S., Ma, Y., Kim, Y., Daniel, A.R., and Kirsch, D.G. (2018). Blocking Cyclin-Dependent Kinase 4/6 During Single Dose Versus Fractionated Radiation Therapy Leads to Opposite Effects on Acute Gastrointestinal Toxicity in Mice. Int. J. Radiat. Oncol. *102*, 1569–1576. https://doi.org/10.1016/j.ijrobp.2018.07.192.

68. Prabakaran, P.J., Javaid, A.M., Swick, A.D., Werner, L.R., Nickel, K.P., Sampene, E., Hu, R., Ong, I.M., Bruce, J.Y., Hartig, G.K., et al. (2017). Radiosensitization of adenoid cystic carcinoma with MDM2 inhibition. Clin. Cancer Res. *23*, 6044–6053. https://doi.org/10.1158/1078-0432.CCR-17-0969.

69. Duy, C., Li, M., Teater, M., Meydan, C., Garrett-Bakelman, F.E., Lee, T.C., Chin, C.R., Durmaz, C., Kawabata, K.C., Dhimolea, E., et al. (2021). Chemotherapy induces senescence-like resilient cells capable of initiating aml recurrence. Cancer Discov. *11*, 1542–1561. https://doi.org/10.1158/2159-8290.CD-20-1375.

70. Dhimolea, E., de Matos Simoes, R., Kansara, D., Al'Khafaji, A., Bouyssou, J., Weng, X., Sharma, S., Raja, J., Awate, P., Shirasaki, R., et al. (2021). An Embryonic Diapause-like Adaptation with Suppressed Myc Activity Enables Tumor Treatment Persistence. Cancer Cell *39*, 240-256.e11. https://doi.org/10.1016/j.ccell.2020.12.002.

71. Chang, C.A., Jen, J., Jiang, S., Sayad, A., Mer, A.S., Brown, K.R., Nixon, A.M.L., Dhabaria, A., Tang, K.H., Venet, D., et al. (2022). Ontogeny and Vulnerabilities of Drug-Tolerant Persisters in HER2+ Breast Cancer. Cancer Discov. *12*, 1022–1045. https://doi.org/10.1158/2159-8290.CD-20-1265.

72. Rehman, S.K., Haynes, J., Collignon, E., Brown, K.R., Wang, Y., Nixon, A.M.L., Bruce, J.P., Wintersinger, J.A., Singh Mer, A., Lo, E.B.L., et al. (2021). Colorectal Cancer Cells Enter a Diapause-like DTP State to Survive Chemotherapy. Cell *184*, 226-242.e21. https://doi.org/10.1016/j.cell.2020.11.018.

73. Ebinger, S., Özdemir, E.Z., Ziegenhain, C., Tiedt, S., Castro Alves, C., Grunert, M., Dworzak, M., Lutz, C., Turati, V.A., Enver, T., et al. (2016). Characterization of Rare, Dormant, and Therapy-Resistant Cells in Acute Lymphoblastic Leukemia. Cancer Cell *30*, 849–862. https://doi.org/10.1016/j.ccell.2016.11.002.

74. Liu, Y., Azizian, N.G., Sullivan, D.K., and Li, Y. (2022). mTOR inhibition attenuates chemosensitivity through the induction of chemotherapy resistant persisters. Nat. Commun. *13*, 7047. https://doi.org/10.1038/s41467-022-34890-6.

75. Boroviak, T., Loos, R., Lombard, P., Okahara, J., Behr, R., Sasaki, E., Nichols, J., Smith, A., and Bertone, P. (2015). Lineage-Specific Profiling Delineates the Emergence and Progression of Naive Pluripotency in Mammalian Embryogenesis. Dev. Cell *35*, 366–382. https://doi.org/10.1016/j.devcel.2015.10.011.

76. Pudlo, P., Marin, J.M., Estoup, A., Cornuet, J.M., Gautier, M., and Robert, C.P. (2016). Reliable ABC model choice via random forests. Bioinformatics *32*, 859–866. https://doi.org/10.1093/bioinformatics/btv684.

77. Lenstra, T.L., Rodriguez, J., Chen, H., and Larson, D.R. (2016). Transcription Dynamics in Living Cells. Annu. Rev. Biophys. *45*, 25–47. https://doi.org/10.1146/annurev-biophys-062215-010838.

78. Batchelor, E., Loewer, A., Mock, C., and Lahav, G. (2011). Stimulus-dependent dynamics of p53 in single cells. Mol. Syst. Biol. *7*, 488. https://doi.org/10.1038/msb.2011.20.

79. Patro, R., Duggal, G., Love, M.I., Irizarry, R.A., and Kingsford, C. (2017). Salmon provides fast and bias-aware quantification of transcript expression. Nat. Methods *14*, 417–419. https://doi.org/10.1038/nmeth.4197.

80. Harrow, J., Frankish, A., Gonzalez, J.M., Tapanari, E., Diekhans, M., Kokocinski, F., Aken, B.L., Barrell, D., Zadissa, A., Searle, S., et al. (2012). GENCODE: The reference human genome

annotation for The ENCODE Project. Genome Res. *22*, 1760–1774. https://doi.org/10.1101/gr.135350.111.

81. Puente-Santamaria, L., Wasserman, W.W., and Del Peso, L. (2019). TFEA.ChIP: a tool kit for transcription factor binding site enrichment analysis capitalizing on ChIP-seq datasets. Bioinformatics *35*, 5339–5340. https://doi.org/10.1093/bioinformatics/btz573.

82. Yan, X., Stuurman, N., Ribeiro, S.A., Tanenbaum, M.E., Horlbeck, M.A., Liem, C.R., Jost, M., Weissman, J.S., and Vale, R.D. (2021). High-content imaging-based pooled CRISPR screens in mammalian cells. J. Cell Biol. *220*, e202008158. https://doi.org/10.1083/jcb.202008158.

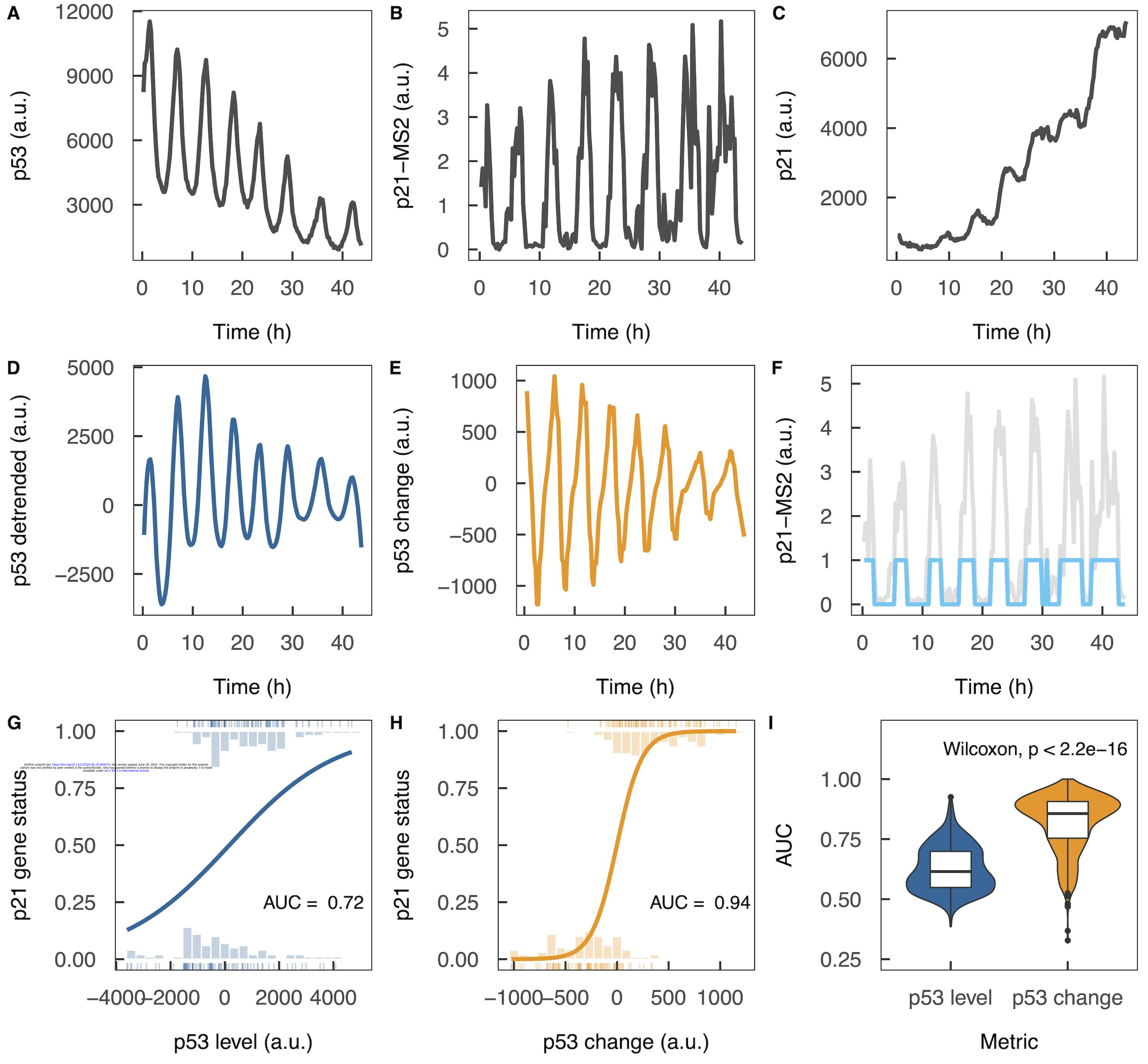

A
p53 (a.u.)
12000
9000
6000
3000
0
10
20
30
40
Time (h)
B
p21−MS2 (a.u.)
5
4
3
2
1
0
Time (h)
C
p21 (a.u.)
6000
4000
2000
Time (h)
D
p53 detrended (a.u.)
5000
2500
0
−2500
Time (h)
E
p53 change (a.u.)
1000
500
0
−500
−1000
Time (h)
F
p21−MS2 (a.u.)
Time (h)
G
p21 gene status
1.00
0.75
0.50
0.25
0.00
AUC = 0.72
−4000
−2000
0
2000
4000
p53 level (a.u.)
H
p21 gene status
AUC = 0.94
−1000
−500
0
500
1000
p53 change (a.u.)
I
AUC
Wilcoxon, p < 2.2e−16
1.00
0.75
0.50
0.25
p53 level
p53 change
Metric


A
Positive Regulation Model
p53
CDKN1A
B
Incoherent Feedforward Loop Model
p53
R
R
p53
R
CDKN1A
C
Fluorescence (a.u.)
Time (h)
D
Fluorescence (a.u.)
Time (h)
E
p21−MS2 autocorrelation
Delay (h)
F
p21−MS2 autocorrelation
Delay (h)
G
p53 − p21−MS2 crosscorrelation
Delay (h)
H
p53 − p21−MS2 crosscorrelation
Delay (h)
I
Data
PR Model
p21−MS2 autocorrelation
Delay (h)
J
Data
PR Model
p53 − p21−MS2 crosscorrelation
Delay (h)
K
Data
IFFL Model
p21−MS2 autocorrelation
Delay (h)
L
Data
IFFL Model
p53 − p21−MS2 crosscorrelation
Delay (h)

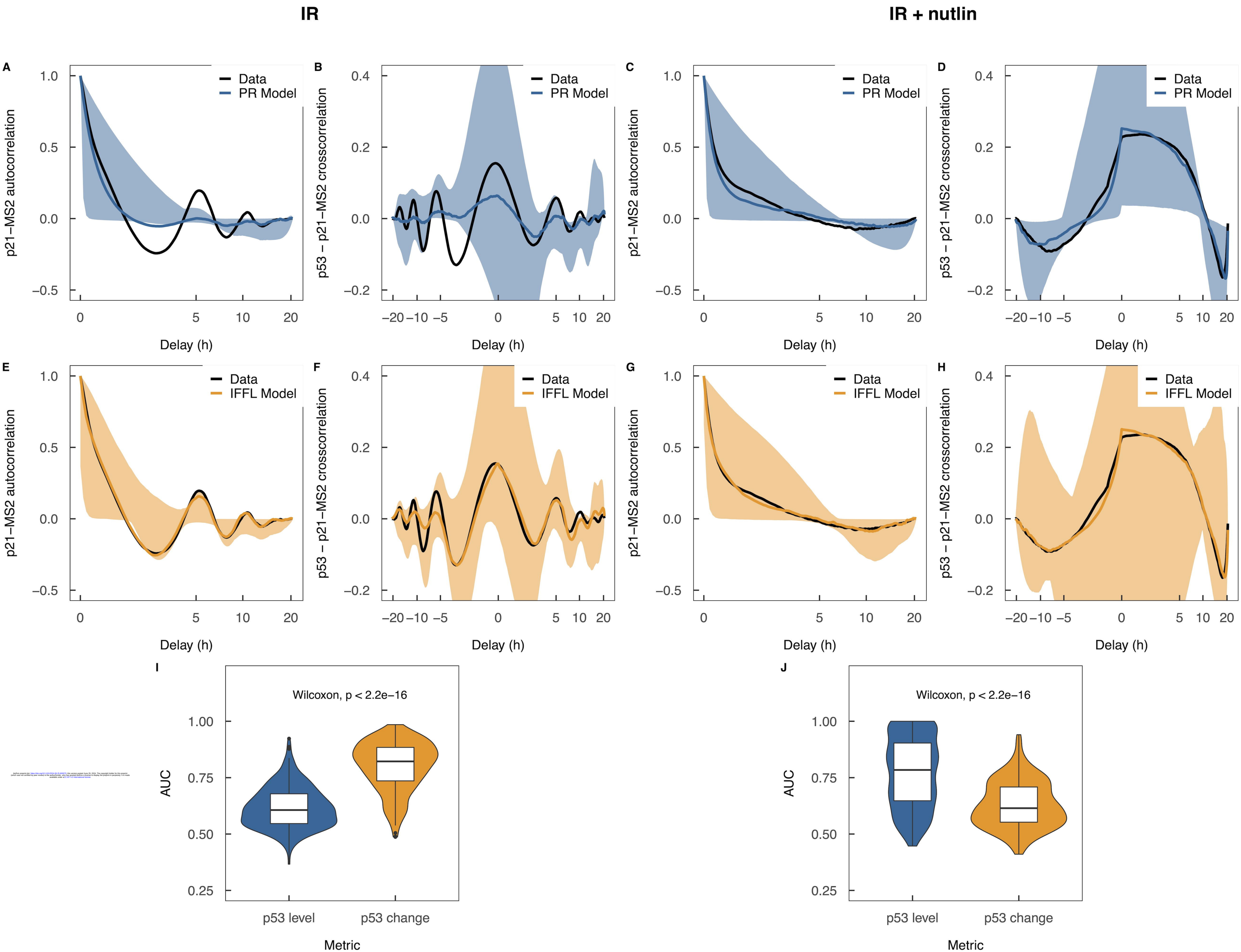

IR
IR + nutlin
A
B
C
D
E
F
G
H
I
J
Data
PR Model
IFFL Model
p21−MS2 autocorrelation
p53 − p21−MS2 crosscorrelation
Delay (h)
Wilcoxon, p < 2.2e−16
AUC
p53 level
p53 change
Metric

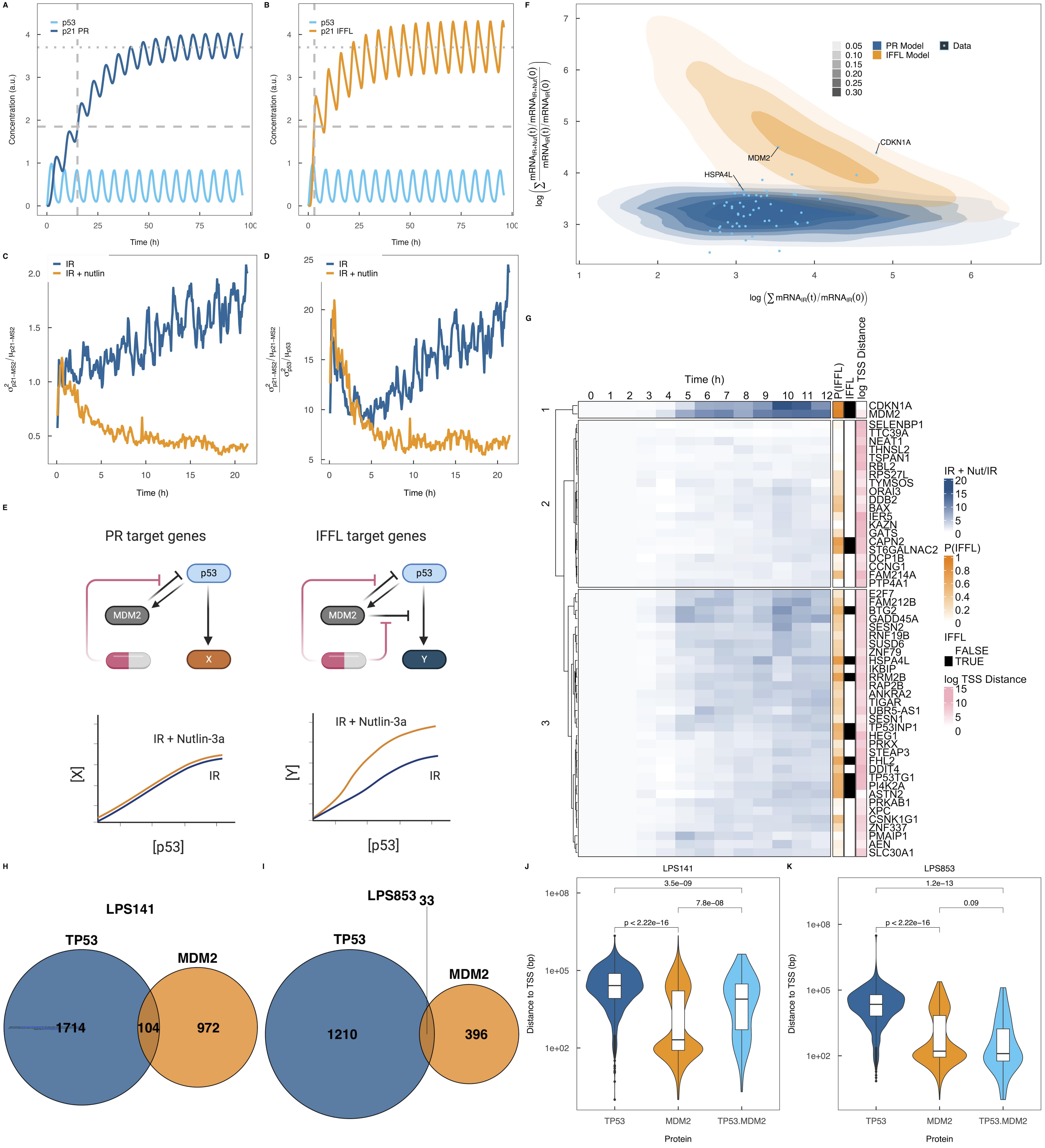

A
p53
p21 PR
Concentration (a.u.)
Time (h)
B
p53
p21 IFFL
Concentration (a.u.)
Time (h)
C
IR
IR + nutlin
Time (h)
D
IR
IR + nutlin
Time (h)
E
PR target genes
p53
MDM2
X
IR + Nutlin-3a
IR
[X]
[p53]
IFFL target genes
p53
MDM2
Y
IR + Nutlin-3a
IR
[Y]
[p53]
F
0.05
0.10
0.15
0.20
0.25
0.30
PR Model
IFFL Model
Data
CDKN1A
MDM2
HSPA4L
G
Time (h)
P(IFFL)
IFFL
log TSS Distance
CDKN1A
MDM2
SELENBP1
TTC39A
NEAT1
THNSL2
TSPAN1
RBL2
RPS27L
TYMSOS
ORAI3
DDB2
BAX
IER5
KAZN
GATS
CAPN2
ST6GALNAC2
DCP1B
CCNG1
FAM214A
PTP4A1
E2F7
FAM212B
BTG2
GADD45A
SESN2
RNF19B
SUSD6
ZNF79
HSPA4L
IKBIP
RRM2B
RAP2B
ANKRA2
TIGAR
UBR5-AS1
SESN1
TP53INP1
HEG1
PRKX
STEAP3
FHL2
DDIT4
TP53TG1
PI4K2A
ASTN2
PRKAB1
XPC
CSNK1G1
ZNF337
PMAIP1
AEN
SLC30A1
IR + Nut/IR
P(IFFL)
IFFL
FALSE
TRUE
log TSS Distance
H
LPS141
TP53
MDM2
1714
104
972
I
LPS853
33
TP53
MDM2
1210
396
J
LPS141
3.5e−09
7.8e−08
p < 2.22e−16
Distance to TSS (bp)
TP53
MDM2
TP53.MDM2
Protein
K
LPS853
1.2e−13
0.09
p < 2.22e−16
Distance to TSS (bp)
TP53
MDM2
TP53.MDM2
Protein


A
1
2
IR
IR + nutlin
log(p21(t))
log(p53(t))
B
slope
y−intercept
IR + nutlin
Mixture Component 2
IR + nutlin
Mixture Component 1
IR
Mixture Component 2
IR
Mixture Component 1
Estimate
C
log(p21) (a.u.)
Time (h)
D
0.16 h^{-1}
3.09 h^{-1}
Density
log(p21 degradation rate) (h^{-1})
E
IR + nutlin
Weighted mean
IR + nutlin
Slow degradation
IR + nutlin
Fast degradation
IR
Weighted mean
IR
Slow degradation
IR
Fast degradation
log(Production rate) (a.u./h)
F
log(p21(t))
log(p53(t))
G
Treatment
Time
Replicate
Treatment
IR
IR + nutlin
GSVA
Time
Replicate
S
G1/S
G2/M
M
M/G1
G0
Time (h)


A
KIF23
UBE2C
LMNB1
ALDH1A3
CCNA2
UBE2T
AQP3
$-\log_{10}(p_{adj})$
Effect size
B
TP53
TP63
Other
$-\log_{10}(p_{adj})$
$\log_2(OR)$
C
E2F4
Other
$-\log_{10}(p_{adj})$
$\log_2(OR)$
D
Treatment
IR
IR + nutlin
GSVA
Time
Replicate
Treatment
Time
Replicate
Duy Chemotherapy Induced Stress Down
Dhimolea Persister Diapause Down
Liu mTOR Persister Down
Chang Mesenchymal Persister Down
Rehman Embryonic Pausing Down
Dhimolea Persister Diapause Up
Boroviak Diapause Up
Liu mTOR Persister Up
Duy Chemotherapy Induced Stress Up
Ebinger Label Retaining Cells
Chang Mesenchymal Persister Up
Duig Slow Cycling Cancer Cells Up
Chang Luminal Persister Up
Rehman Embryonic Pausing Up
Chang Luminal Persister Down
Time (h)
E
100 200 300 400
Downregulated Signature
Upregulated Signature
Weighted Mean
urinary_tract
upper_aerodigestive_tract
stomach
soft_tissue
skin
pancreas
ovary
oesophagus
lung
liver
large_intestine
kidney
endometrium
central_nervous_system
breast
bone
Primary Site
Coefficient
F
< Median
>= Median
Recurrence-Free Survival
p = 0.021
Time (months)
G
< Median
>= Median
Overall Survival
p = 0.021
Time (months)


A
B
C
Time (h)
0 3 6 9 12 15 18 21 24 27 30 33 36 39 42
10 Gy
5 Gy
2.5 Gy
Cell
p53
p21-MS2
p21
D
E
F
G
H
I
J
p53 (a.u.)
p21−MS2 (a.u.)
Wilcoxon, p < 2.2e−16
AUC
p53 level
p53 change
Metric

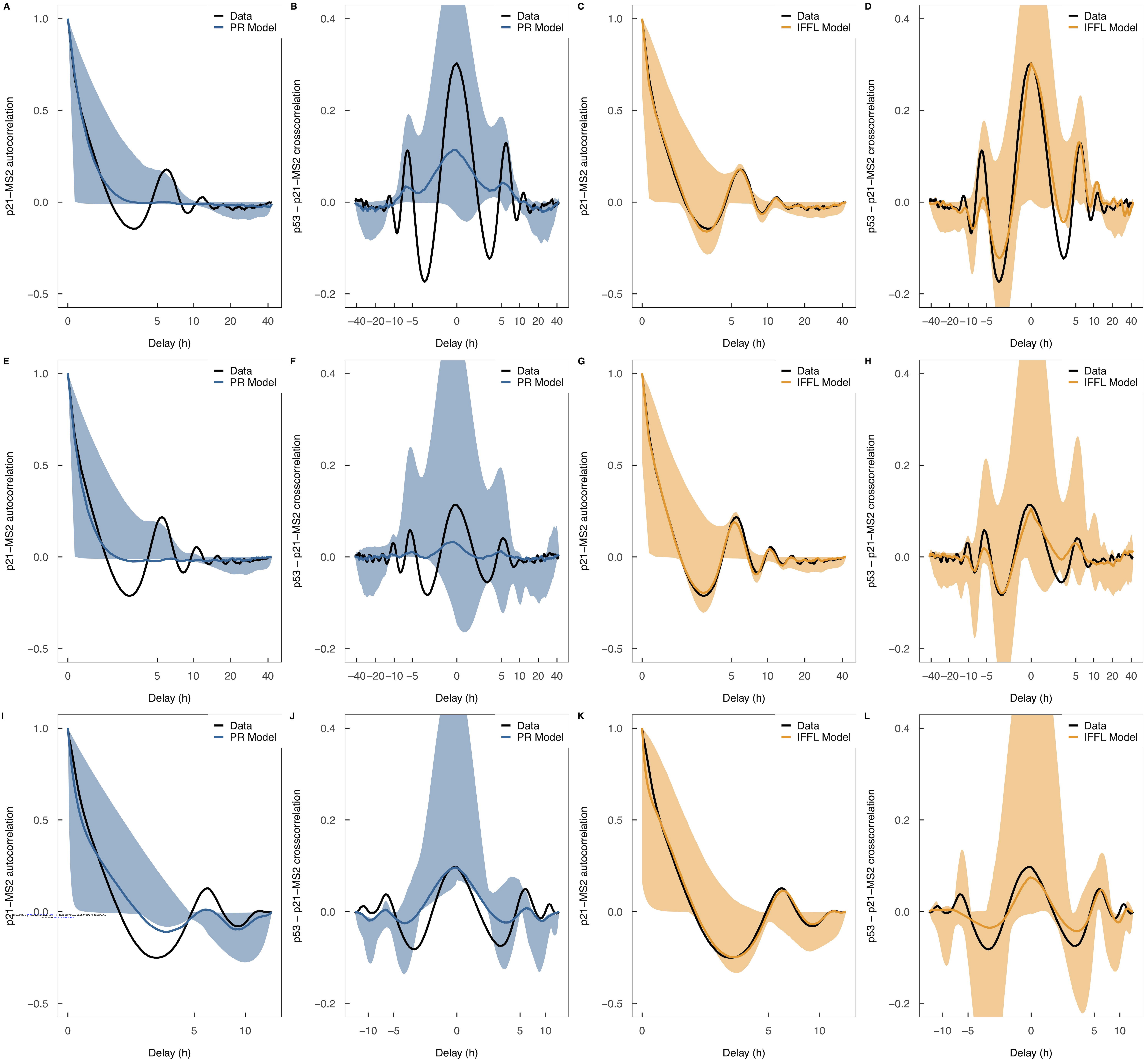

A
B
C
D
E
F
G
H
I
J
K
L
Data
PR Model
IFFL Model
p21−MS2 autocorrelation
p53 − p21−MS2 crosscorrelation
Delay (h)
1.0
0.5
0.0
−0.5
0.4
0.2
−0.2
0
5
10
20
40
−40
−20
−10
−5


A
B
C
Time (h)
0
3
6
9
12
15
18
21
IR
IR + nutlin
Cell
p53
6
4
2
0
-2
p21-MS2
2
1.5
1
0.5
0
-0.5
p21

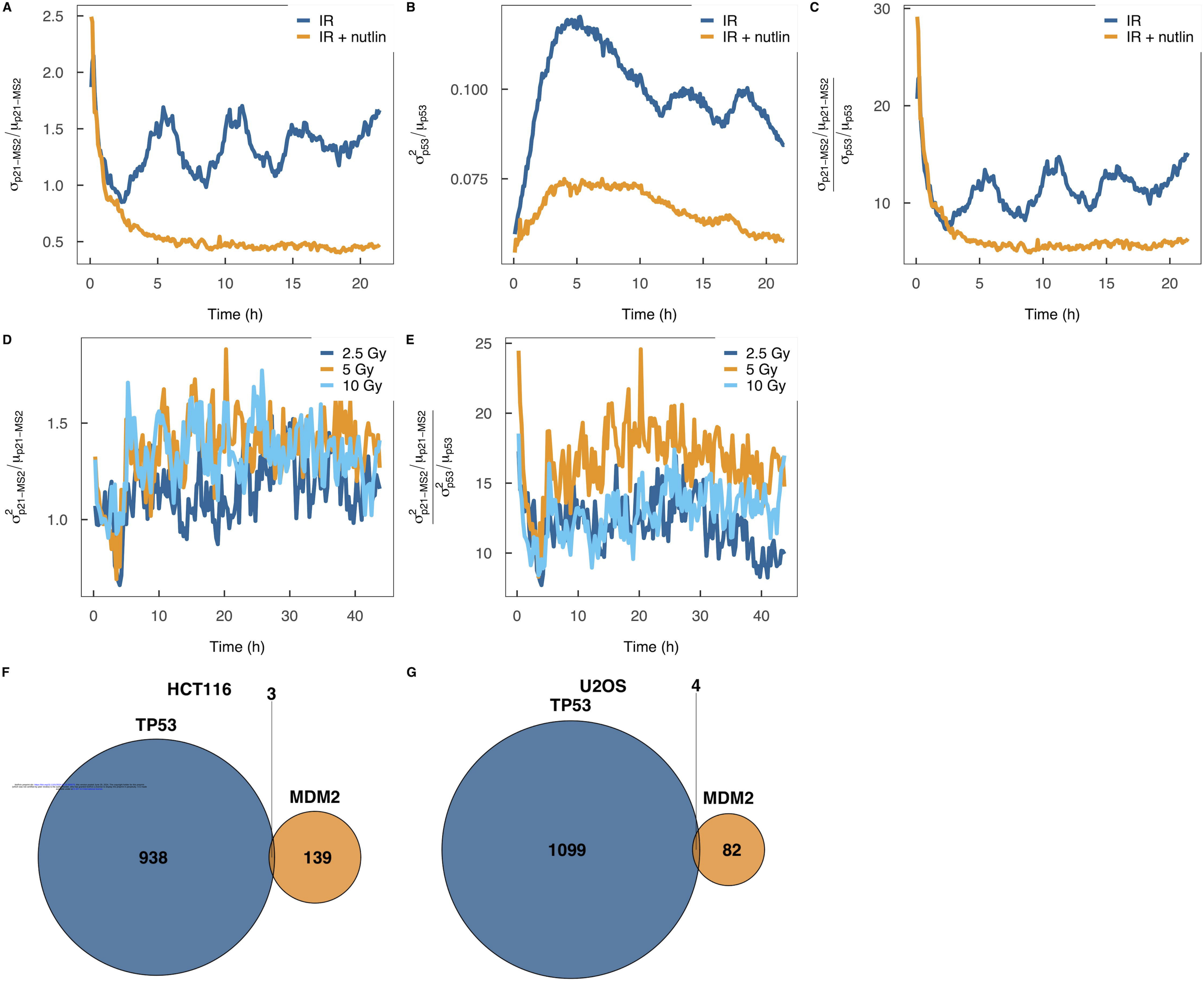
A
B
C
D
E
F
G
IR
IR + nutlin
2.5 Gy
5 Gy
10 Gy
Time (h)
HCT116
U2OS
TP53
MDM2
938
3
139
1099
4
82


A
Time (h)
0 3 6 9 12 15 18 21 24 27 30 33 36 39 42
p53 siRNA p21 siRNA
Cell
p21 siRNA
Cell
p21
4
2
0
-2
-4
B
log(p21(t))
log(p53(t))
C
IR
IR + nutlin
Area (a.u.)
Time (h)
D
IR
IR + nutlin
p = <2e−16
p = 7.2e−06
Nuclear area (a.u.)
0 h
21 h
Time
E
Treatment
IR
IR + nutlin
GSVA
Time
Replicate
Treatment
Time
Replicate
FSC Screen
Nuclear Size Screen Validated Hits
H2B−mGFP Screen
Nuclear Size Screen
Time (h)

A
Treatment
Time
Replicate
E2F Targets
G2M Checkpoint
MYC Targets V2
MYC Targets V1
Pancreas Beta Cells
Spermatogenesis
MTORC1 Signaling
Unfolded Protein Response
DNA Repair
Fatty Acid Metabolism
Oxidative Phosphorylation
Reactive Oxygen Species Pathway
KRAS Signaling Down
Myogenesis
Coagulation
Apical Junction
Hypoxia
NOTCH Signaling
Apical Surface
Allograft Rejection
KRAS Signaling Up
Inflammatory Response
IL6 JAK STAT3 Signaling
Epithelial Mesenchymal Transition
Apoptosis
Angiogenesis
TGF Beta Signaling
Bile Acid Metabolism
Peroxisome
Interferon Gamma Response
Interferon Alpha Response
Xenobiotic Metabolism
Adipogenesis
Glycolysis
WNT Beta Catenin Signaling
Estrogen Response Early
UV Response Up
Estrogen Response Late
Cholesterol Homeostasis
IL2 STAT5 Signaling
PI3K AKT MTOR Signaling
Complement
Heme Metabolism
UV Response Down
Hedgehog Signaling
Mitotic Spindle
TNFA Signaling Via NFKB
P53 Pathway
Androgen Response
Protein Secretion
Treatment
IR
IR + nutlin
GSVA
1
0.5
0
−0.5
−1
Time
12
10
8
6
4
2
Replicate
1
2
3 4 5 6 7 8 9 10 11 12
Time (h)
B
Recurrence−Free Survival
< Median
>= Median
p = 0.00071
Time (months)
C
Overall Survival
< Median
>= Median
p = 0.0055
Time (months)
D
Recurrence−Free Survival
< Median
>= Median
p = 0.051
Time (months)
E
Overall Survival
< Median
>= Median
p = 0.044
Time (months)
F
Recurrence−Free Survival
< Median
>= Median
p = 0.7
Time (months)
G
Overall Survival
< Median
>= Median
p = 0.39
Time (months)